Monthly Notices of the ROYAL ASTRONOMICAL SOCIETY

MNRAS **512,** 3717–3737 (2022) https://doi.org/10.1093/mnras/stac663
Advance Access publication 2022 March 12

Cold and hot gas distribution around the Milky-Way – M31 system in the HESTIA simulations

Mitali Damle [1]★ Martin Sparre [1,2] Philipp Richter,[1] Maan H. Hani [3]† Sebastián E. Nuza,[4,5] Christoph Pfrommer [2] Robert J. J. Grand [6,7,8] Yehuda Hoffman,[9] Noam Libeskind,[2] Jenny G. Sorce,[2,10] Matthias Steinmetz,[2] Elmo Tempel [11,12] Mark Vogelsberger [13] and Peng Wang[2]

[1]*Institut für Physik und Astronomie, Universität Potsdam, Campus Golm, Haus 28, Karl-Liebknecht Straße 24-25, D-14476 Potsdam, Germany*
[2]*Leibniz-Institut für Astrophysik Potsdam (AIP), An der Sternwarte 16, D-14482 Potsdam, Germany*
[3]*Department of Physics and Astronomy, McMaster University, Hamilton Ontario L8S 4M1, Canada*
[4]*Instituto de Astronomía y Física del Espacio (IAFE, CONICET-UBA), CC 67, Suc. 28, 1428 Buenos Aires, Argentina*
[5]*Facultad de Ciencias Exactas y Naturales (FCEyN), Universidad de Buenos Aires (UBA), 1428, Buenos Aires, Argentina*
[6]*Max-Planck-Institut für Astrophysik, Karl-Schwarzschild-Str 1, D-85748 Garching, Germany*
[7]*Instituto de Astrofísica de Canarias, Calle Váa Láctea s/n, E-38205 La Laguna, Tenerife, Spain*
[8]*Departamento de Astrofísica, Universidad de La Laguna, Av. del Astrofísico Francisco Sánchez s/n, E-38206 La Laguna, Tenerife, Spain*
[9]*Racah Institute of Physics, Hebrew University, 91904 Jerusalem, Israel*
[10]*Centre de Recherche Astrophysique de Lyon, Univ Lyon, ENS de Lyon, Univ Lyon1, CNRS, UMR5574, F-69007 Lyon, France*
[11]*Tartu Observatory, University of Tartu, Observatooriumi 1, 61602 Tõravere, Estonia*
[12]*Estonian Academy of Sciences, Kohtu 6, 10130 Tallinn, Estonia*
[13]*Department of Physics, Kavli Institute for Astrophysics and Space Research, Massachusetts Institute of Technology, Cambridge, MA 02139, USA*

Accepted 2022 March 3. Received 2022 March 3; in original form 2021 July 14

ABSTRACT

Recent observations have revealed remarkable insights into the gas reservoir in the circumgalactic medium (CGM) of galaxy haloes. In this paper, we characterize the gas in the vicinity of Milky Way and Andromeda analogues in the HESTIA (High resolution Environmental Simulations of The Immediate Area) suite of constrained Local Group (LG) simulations. The HESTIA suite comprise of a set of three high-resolution AREPO-based simulations of the LG, run using the Auriga galaxy formation model. For this paper, we focus only on the $z = 0$ simulation data sets and generate mock skymaps along with a power spectrum analysis to show that the distributions of ions tracing low-temperature gas (H I and Si III) are more clumpy in comparison to warmer gas tracers (O VI, O VII, and O VIII). We compare to the spectroscopic CGM observations of M31 and low-redshift galaxies. HESTIA underproduces the column densities of the M31 observations, but the simulations are consistent with the observations of low-redshift galaxies. A possible explanation for these findings is that the spectroscopic observations of M31 are contaminated by gas residing in the CGM of the Milky Way.

Key words: software: data analysis – software: simulations – Galaxy: evolution – galaxies: evolution – galaxies: Local Group.

1 INTRODUCTION

Our understanding of the tenuous gas reservoir surrounding galaxies, better known as the circumgalactic medium (CGM), has dramatically improved since its first detection, back in the 1950s (Spitzer 1956; Münch & Zirin 1961; Bahcall & Spitzer 1969). The CGM is a site through which pristine, cold intergalactic medium (IGM) gas passes on its way into the galaxy and it is also the site where metal-enriched gas from the interstellar medium (ISM) gets dumped via outflows and winds (Anglés-Alcázar et al. 2017; Suresh et al. 2019). CGM gas is often extremely challenging to detect in emission due to its low-column densities. Therefore, most of our knowledge about its nature stems from absorption line studies (Werk et al. 2014; Tumlinson, Peeples & Werk 2017) of quasar sightlines passing through the CGM of foreground galaxies.

Observational data sets from instruments like Far Ultraviolet Spectroscopic Explorer (FUSE; see Moos et al. 2000; Savage et al. 2000; Sembach et al. 2000), Space Telescope Imaging Spectrograph (*HST*-STIS; see Kimble et al. 1998; Woodgate et al. 1998) and Cosmic Origins Spectrograph (*HST*-COS; see Froning & Green 2009; Green et al. 2011) have revolutionized our understanding of not just the MW CGM but the CGMs of other galaxies as well (Richter et al. 2001; Lehner et al. 2012; Herenz et al. 2013; Tumlinson et al. 2013; Werk et al. 2013; Fox et al. 2014; Werk et al. 2014; Richter et al. 2017).

Numerous studies through the last decade involving quasar absorption line studies of various low and intermediate ions tracing a substantial range in temperatures and densities have revealed the complex, multiphase structure of the CGM (Nielsen et al. 2013; Tumlinson et al. 2013; Bordoloi et al. 2014; Richter et al. 2016; Lehner et al. 2018). Lehner et al. (2020) have gone a step

★ E-mail: damle@uni-potsdam.de
† Herschel fellow.

ahead in quasar absorption line studies by obtaining multi-ion deep observations of several sightlines heterogeneously piercing the CGM of a single galaxy (M31).

Recent studies conclude that a significant percentage of galactic baryons could lie in the warm–hot virialized gas phase (Peeples et al. 2014; Tumlinson et al. 2017), increasingly emphasizing the importance of high ions in describing the CGM mass budget (Tumlinson et al. 2017). O VI, which is an important tracer of the warm–hot CGM ($T \sim 10^{5.5}$ K), has been detected in gas reservoirs around star-forming galaxies in Far UV (Tumlinson et al. 2011). Even hotter CGM gas, traced primarily by O VII and O VIII, has been detected around galaxies in X-ray studies (Das et al. 2019b; Das et al. 2020). Apart from these high ions, Coronal Broad Lyman alpha absorbers could also contribute towards constituting the hot CGM (Richter 2020).

Significant progress is also being made via systematic CGM studies targeting diverse galaxy samples which provide insightful views into the synergy between the CGM and the evolution of its host galaxy. The presence of warm gas clouds around late-type galaxies at low redshift (Stocke et al. 2013), the impact of starbursts (Borthakur et al. 2013) and AGN (Berg et al. 2018), evidence of a bimodal metallicity distribution in the form of metal-poor pristine and metal-rich recycled gas streams (Lehner et al. 2013) have given us a peek into the interplay between the CGM and its parent galaxy. The theory of galactic winds injecting metal-rich gas from the ISM out to the CGM (Ford et al. 2013; Hummels et al. 2013) is now being supported by observational evidence (Rupke et al. 2019).

Despite all the advancements in the past few years, limited sightline observations and our technological inability to probe substantially lower column densities in the CGM of other galaxies indicate that we cannot yet fully rely solely on these studies to give us a complete picture of the workings of the CGM (Tumlinson et al. 2017). Therefore, studying the MW and the LG CGM (which will always have better CGM data sets as compared to those for non-LG galaxies) assumes a great importance in this context.

High-velocity warm O VI gas has been observed extensively around the MW (Savage et al. 2003; Sembach et al. 2003; Wakker et al. 2003). *HST* UV spectra of a list of low and intermediate ions have further helped us track the expanse of high-velocity clouds (HVCs) around our Galaxy (Lehner et al. 2012; Herenz et al. 2013). A low-velocity cool-ionized CGM component has also been detected recently around the MW (Zheng et al. 2019; Bish et al. 2021). Additionally, a long hypothesized hot diffuse galactic gas phase (Gupta et al. 2012) has been observed using the highly ionized O VII and O VIII ions (Miller & Bregman 2015; Das et al. 2019a). While the observations of the Galaxy's CGM certainly provide us with more sightlines and enable us to detect slightly lower column densities as compared to other galaxies' CGMs, galactic CGM observations are fraught with a greater possibility of contamination from sources lying in the line-of-sight of our observations, thereby masking the true nature of our Galaxy's CGM.

With the advent of the above observations, complementary studies with regards to the CGMs around the galaxies, generated using cosmological galaxy formation simulations, started gaining momentum (Vogelsberger et al. 2020). Cosmological simulations, in general, have been extremely successful in replicating many pivotal observational properties central to the current galaxy formation and evolution model (Vogelsberger et al. 2014a,b). These include galaxy morphologies (Ceverino, Dekel & Bournaud 2010; Aumer et al. 2013; Marinacci, Pakmor & Springel 2014; Somerville & Davé 2015; Grand et al. 2017), galaxy scaling relations (Booth & Schaye 2009; Angulo et al. 2012; Vogelsberger et al. 2013), M_*–$M_{\rm halo}$ relationship (Behroozi, Conroy & Wechsler 2010; Moster, Naab & White 2013), and star formation in galaxies (Behroozi, Wechsler & Conroy 2013; Agertz & Kravtsov 2015; Furlong et al. 2015; Sparre et al. 2015, 2017; Donnari et al. 2019). Like observations, cosmological simulations provide different approaches to quantify the typical baryon and metal budgets of galaxies (Ford et al. 2014; Schaye et al. 2015; Suresh et al. 2016; Hani et al. 2019; Tuominen et al. 2021). They reveal how the motions of gas manifests itself in various forms like inflow streams from the IGM, or replenished outflows from the galaxy out to its CGM, or stellar winds or supernovae and AGN feedback (Nelson et al. 2019; Appleby et al. 2021; Wright et al. 2021).

Given that the computational studies of the CGM have provided an enormous insight into the evolution of galaxies, it is worthwhile to look back to our local environment, i.e. the Local Group (LG). Apart from tracking the formation history of MW–M31 (Hammer et al. 2013; Ibata et al. 2013; Scannapieco et al. 2015) and the accretion histories of MW-like galaxies (Nuza et al. 2019), our LG, over the past decade, has proved to be an ideal site for studies involving ΛCDM model tests (Klypin et al. 1999; Wetzel et al. 2016; Lovell et al. 2017), dwarf galaxy formation and evolution (Tolstoy, Hill & Tosi 2009; Garrison-Kimmel et al. 2014; Pawlowski, Ibata & Bullock 2017; Samuel et al. 2020), effects of environment on star formation histories of MW-like galaxies (Creasey et al. 2015), local Universe re-ionization (Ocvirk et al. 2020), and the cosmic web (Nuza et al. 2014; Forero-Romero & González 2015; Metuki et al. 2015). Observational constraints of the Local Universe have resulted in an emergence of constrained simulations, where the large-scale structure resembles the observations (Nuza, Dolag & Saro 2010; Knebe et al. 2011; Libeskind et al. 2011; Di Cintio et al. 2013; Nuza et al. 2013). It is also worthwhile to note that such LG constrained simulations might be the set-ups best equipped to separate out any sources of possible contamination towards the MW CGM.

A simulation of a Milky-Way-like galaxy in a constrained environment was done by the CLUES (Constrained Local UniversE Simulations) project (Gottlöber, Hoffman & Yepes 2010), which were one of the first cosmological simulations to include a realistic local environment within the large-scale LG structure. Nuza et al. (2014) carried out a study on the $z = 0$ gas distribution around MW and M31 in the CLUES simulation to characterize the effect of cosmography on the LG CGM. They analysed the cold and hot gas phases, computed their masses and accretion/ejection rates, and later compared their results with the absorption-line observations from Richter et al. (2017).

We build upon the approach adopted in Nuza et al. (2014) by analysing the constrained LG simulations, HESTIA (Libeskind et al. 2020), which in comparison to the original CLUES simulations have better constrained initial conditions. In HESTIA we, furthermore, use the Auriga galaxy formation model (Grand et al. 2017), which produces realistic Milky-Way-mass disc galaxies. In comparison to the previous CLUES simulations, we carry out a more extensive analysis to predict column densities of a range of tracer ions (H I, Si III, O VI, O VII, and O VIII) selected to give a complete view of the various gas phases in and around the galaxies. This helps us, for example, with the interpretation of absorption studies of the LG CGM gas.

The aim of this paper is to provide predictions for absorption-line observations of the gas in the LG. We achieve this by studying the gas around LG galaxies in the state-of-the-art constrained magnetohydrodynamical (MHD) simulations, HESTIA (High resolution Environmental Simulations of The Immediate Area). The comparison between HESTIA and some of the recent observations makes it possible to constrain the galaxy formation models of our simulations.

This paper is structured as follows: Section 2 describes the analysis tools and the simulation. We present our results in Section 3, which include Mollweide projection maps (Section 3.1), power spectra (Section 3.3), and radial column density profiles (Section 3.4). We compare our results with some of the recent observations and other simulations in Sections 3.5 and 3.6. Further, we discuss the implications of our results in the context of current theories about CGM and galaxy formation and evolution in Section 4. We also analyse the possibility of MW's CGM gas interfering with M31's CGM observations in Section 4.1. Finally, we sum up our conclusions and provide a quick note about certain caveats and ideas to be implemented in future projects (Section 5).

2 METHODS

We use three high resolution realizations from the HESTIA suite, a set of intermediate and high resolution cosmological magneto-hydrodynamical constrained simulations of the LG, analysed only at the present time ($z = 0$). The HESTIA project is a part of the larger CLUES collaboration (Gottlöber et al. 2010; Libeskind et al. 2010; Sorce et al. 2015; Carlesi et al. 2016), whose principal aim is to generate constrained simulations of the local Universe in order to match the mock observational outputs with real observations from our galactic neighbourhood.

The following subsection summarizes the technical specifications of these simulations. A more extensive description of the simulations can be found in the official HESTIA release paper (Libeskind et al. 2020).

2.1 Simulations

2.1.1 Initial conditions

The small-scale initial conditions are obtained from a sampling of the peculiar velocity field. The CosmicFlows-2 catalogue (Tully et al. 2013), used to derive peculiar velocities, provides constraints up to distances farther than that was available for the predecessor CLUES simulation. Reverse Zel'dovich technique (Doumler et al. 2013) handles the cosmic displacement field better, hence offering smaller structure shifts. A new technique, bias minimization scheme (Sorce 2015), has been employed for HESTIA simulations to ensure that the LG characteristic objects (e.g. Virgo cluster) have proper mass. The above mentioned new elements (see Sorce et al. 2015 for further details) in conjunction with the earlier aspects of constrained realization (Hoffman & Ribak 1991) and Wiener Filter (Sorce et al. 2013) offer HESTIA a clear edge over the previous generation CLUES simulations.

Low-resolution, constrained, dark-matter only simulations are the fields from which halo pairs resembling our LG were picked up for intermediate and high-resolution runs. Note that only the highest resolution realizations (those labelled 09–18, 17–11, and 37–11) are used for our analysis in this paper. The first and second numbers in the simulation nomenclature represent the seed for long and short waves, respectively, both of which together constitute to the construction of the initial conditions. Two overlapping 2.5 h^{-1} Mpc spheres centred on the two largest $z = 0$ LG members (MW and M31) represent the effective high-resolution fields which are populated with 8192^3 effective particles. The mass resolution for the DM particles (gas cells) in the high-resolution simulations is 1.5×10^5 $M_\odot$ (2.2×10^4 $M_\odot$), while the softening length (ϵ) for the DM is 220 pc.

While the entire process of selecting cosmographically correct halo pairs involves handpicking MW–M31 candidates with certain criteria (halo mass, separation, isolation) that lie within the corresponding observational constraints, there are yet a few other bulk parameters (M_* versus $M_{\rm halo}$, circular velocity profile) and dynamical properties (total relative velocities) which are organically found to agree well with observations (Guo et al. 2010; Van der Marel et al. 2012; McLeod et al. 2017).

2.1.2 Galaxy formation model

The moving-mesh magneto-hydrodynamic code, AREPO (Springel 2010; Pakmor et al. 2016), has been employed for the higher resolution runs. AREPO, which is based on a quasi-Lagrangian approach, uses an underlying Voronoi mesh (in order to solve the ideal MHD equations) that is allowed to move along the fluid flow, thus seamlessly combining both Lagrangian as well as Eulerian features in a single cosmological simulation. The code follows the evolution of magnetic fields with the ideal MHD approximation (Pakmor, Bauer & Springel 2011; Pakmor & Springel 2013) that has been shown to reproduce several observed properties of magnetic fields in galaxies (Pakmor et al. 2017, 2018) and the CGM (Pakmor et al. 2020). Cells are split (i.e. refined) or merged (i.e. de-refined) whenever the mass of a particular mesh cell varies by more than a factor of two from the target mass resolution.

We adopt the Auriga galaxy formation model (Grand et al. 2017). A two-phase model is used to describe the interstellar medium (ISM), wherein a fraction of cold gas and a hot ambient phase is assigned to each star-forming gas cell (Springel & Hernquist 2003). This two-phase model is enabled for gas denser than the star formation threshold (0.13 cm^{-3}). Energy is transferred between the two phases by radiative cooling and supernova evaporation, and the gas is assumed to be in pressure equilibrium following an effective equation of state (similar to fig. 4 in Springel, Di Matteo & Hernquist 2005). Stellar population particles are formed stochastically from star-forming cells. Black holes (BH) formation and their subsequent feedback contributions are also included in the Auriga framework. Magnetic fields are included as uniform seed fields at the beginning of the simulation runs ($z = 127$) with a comoving field strength of 10^{-14} G, which are amplified by an efficient turbulent dynamo at high redshifts (Pakmor et al. 2017). Gas cooling via primordial and metal cooling (Vogelsberger et al. 2013) and a spatially uniform UV background (Faucher-Giguère et al. 2009) are included. Our galaxy formation model produces a magnetized CGM with a magnetic energy, which is an order of magnitude below the equipartition value for the thermal and turbulent energy density (Pakmor et al. 2020).

In our galaxy formation model, the CGM experiences heating primarily from sources such as SNe Type II, AGN feedback (see fig. 17 in Grand et al. 2017), stellar winds and time-dependent spatially uniform UV background. Stellar and AGN feedback are especially important since they heat and deposit a substantial amount of metals as well as some baryonic material into the CGM (Bogdán et al. 2013; Vogelsberger et al. 2013).

We do not include extra-planar type Ia SNe or runaway type II SNe. We expect the uncertainty due to not including these in our physics model to be extremely small with respect to that due to treating the ISM with an effective equation of state (see for example fig. 10 in Marinacci et al. 2019).

Quasar mode feedback is known to suppress star formation in the inner disc of galaxies (particularly relevant at early times), while the radio mode feedback is known to control the ability of halo gas to cool down efficiently at late times (hence relevant in the context of this study). In general, radio mode feedback is instrumental in keeping the halo gas hot, which in turn results in lesser cool gas in

Table 1. Properties of MW and M31 analogues at $z = 0$ for the three LG HESTIA simulations. The simulations are referred to as 09–18, 17–11 and 37–11, following the nomenclature used in Libeskind et al. 2020 (see also Section 2.1.1). We show the *LG distance* (defined as the distance of a galaxy from the geometric centre of the line that connects MW and M31), the mass in stars and gas bound to each galaxy, and R_{200} and M_{200} of each galaxy. SFR is the star formation rate for all the gas cells within twice the stellar half mass radius. $Z_{\rm SFR}/Z_\odot$ is the SFR-weighted gas metallicity, normalized with respect to the solar metallicity. We also list the observational estimates for MW from Bland-Hawthorn & Gerhard (2016) as well as that for M31. The observational estimate for R_{200} of the MW is calculated as $R_{200} = 1.3 \times R_{\rm vir}$ (following Van der Marel et al. 2012) from the $R_{\rm vir}$ value for MW given in Bland-Hawthorn & Gerhard (2016).

	09–18		17–11		37–11		Obs. estimates for MW	Obs. estimates for M31
	MW	M31	MW	M31	MW	M31	(from Bland-Hawthorn & Gerhard 2016)	
LG distance (kpc)	433.19	433.19	338.01	338.01	425.29	425.29	–	–
log M_* ($M_\odot$)	10.91	11.11	11.06	11.08	10.77	10.72	10.69 ± 0.088	10.84–11.10[1]
log $M_{\rm gas}$ ($M_\odot$)	11.08	11.20	10.92	11.21	10.76	10.87	10.92 ± 0.067	9.78[2]
log M_{200} ($M_\odot$)	12.29	12.33	12.30	12.36	12.00	12.013	12.05 ± 0.096	12.10[3]
R_{200} (kpc)	262.54	270.40	264.48	277.46	211.25	212.81	216.93 ± 23.075	230[3]
log $M_{\rm BH}$ ($M_\odot$)	8.1314	8.277	7.7362	8.1838	7.7787	7.5840	6.6232 ± 0.02	8.15[4]
SFR ($M_\odot$ yr^{-1})	9.476	3.757	3.600	4.754	1.193	2.337	1.650 ± 0.19	0.25–1.0[5]
M_*/SFR (Gyr)	8.577	34.29	31.89	25.29	49.36	22.46	–	–
$Z_{\rm SFR}/Z_\odot$	3.26	3.04	3.55	3.05	3.26	3.31	–	–

Notes. [1]Sick et al. (2015), Rahmani, Lianou & Barmby (2016)
[2]Yin et al. (2009)
[3]Lehner et al. (2020)
[4]Schiavi, Riccardo et al. (2020)
[5]Williams (2003), Williams (2003), Barmby et al. (2006), Tabatabaei & Berkhuijsen (2010), Ford et al. (2013), Lewis et al. (2015), Rahmani et al. (2016), Boardman et al. (2020)

the CGM (see fig. 17 from Grand et al. 2017; also fig. 9 from Irodotou et al. 2021). Hani et al. 2019 studied the effect of AGN feedback on the ionization structure within the CGM of a sample of MW-like galaxies from the Auriga simulations. On the whole, they concluded that in comparison to the galaxies without any AGN feedback, the CGMs of galaxies with an AGN feedback exhibited lesser column densities for low and intermediate ions, while the column densities for high ions remained largely unchanged. While the presence of an ionizing AGN radiation field in the CGM is responsible for slightly reduced abundances of low ions, the abundances of high ions like O VI mainly arise from the halo virial temperatures and are hence, largely unaffected by the AGN feedback effects.

We use the SUBFIND halo finder (Springel et al. 2001; Dolag et al. 2009; Springel et al. 2021) to identify galaxies and galaxy groups in our analysis. When the simulations were run, black holes were seeded in haloes identified by SUBFIND.

Our simulations and analysis consistently use the Planck 2014 best-fitting cosmological parameters (Planck Collaboration XVI 2014), which have the following values: $H_0 = 100\,h$ km s^{-1} Mpc^{-1}, where $h = 0.677$, $\sigma_8 = 0.83$, $\Omega_\Lambda = 0.682$, $\Omega_{\rm M} = 0.270$, and $\Omega_{\rm b} = 0.048$.

2.1.3 *Global properties of the HESTIA analogues*

Table 1 lists key properties for the three realizations of the MW–M31 analogues, which we consider in this paper. We define R_{200} as the radius within which the spherically averaged density is 200 times the critical density of the Universe. M_{200} is the total mass within R_{200}. The overall M_{200}, M_*, $M_{\rm gas}$ and R_{200} values for our MW–M31 analogues are broadly consistent with typical observational estimates (see fig. 7 in Libeskind et al. 2020; see also Yin et al. 2009; Bland-Hawthorn & Gerhard 2016). Among the two most massive galaxies in each of our LG simulations, the galaxy with a larger value of M_{200} is identified as M31, while the other galaxy is identified as MW.

The HESTIA MW analogues reveal $M_{\rm BH}$ values an order of magnitude larger than that stated in the observations of Bland-Hawthorn & Gerhard (2016). This does not, however, necessarily mean that the AGN feedback has been too strong during the simulations, because we see realistic MW stellar masses at $z = 0$. For the CGM, which we study extensively in this paper, the overestimated MW BH masses therefore do not necessarily indicate too strong AGN feedback. We also note that our MW analogues are still consistent with MW-mass galaxies (see fig. 5 of Savorgnan et al. 2016).

Similarly, the SFR at $z = 0$ is also comparable to or larger than observed. We note that the SFR of M31 is larger by a factor of a few in HESTIA in comparison to observations. The generation of winds is closely tied to the SFR in our simulations, so it is possible that the role of outflows is overestimated by HESTIA in comparison to the $z = 0$ observations of M31. Integrated over the lifetime of the galaxies, HESTIA does, however, produce realistic stellar masses at $z = 0$.[1] We therefore do not regard the discrepancy between the $z = 0$ SFR as more problematic than the uncertainty already in place by using an effective model of winds, or, for example, by the simulated M31 galaxies having different merger histories or disc orientations than the *real* M31. In comparison to the SFR values from Bland-Hawthorn & Gerhard 2016, other observational studies report slightly larger SFR values for MW (1–3 $M_\odot$ yr^{-1}, 3–6 $M_\odot$ yr^{-1}, 1–3 $M_\odot$ yr^{-1}, 1.9 ± 0.4 $M_\odot$ yr^{-1}: McKee & Williams 1997; Boissier & Prantzos 1999; Wakker et al. 2007, 2008; Chomiuk & Povich 2011), but these are nevertheless lower than the HESTIA values. We also notice that the MW analogue in the 09–18 simulation exhibits a substantially higher SFR than others. However, all M_*/SFR values (except those for the MW analogue in 09–18 simulation) for our sample are still well within the observational constraints of normal star-forming galaxies with masses comparable to the MW and M31 (see fig. 8 in Speagle et al. 2014). Thus, overall, the HESTIA galaxies seem to be slightly

[1] At a speculative node, it is possible that a too high SFR could be compensated by too high AGN feedback, and this would result in a stellar mass consistent with observations but at the same time a too massive BH mass. Addressing such a hypothesis would require running additional simulations which is beyond the scope of this paper.

Table 2. For the ions considered in our ionization analysis, we list the wavelength of the strongest tracer ion transitions, the ionization energy, characteristic temperature and characteristic density (we quote the ionization energy values from Edlén 1979; Martin & Zalubas 1983; Johnson & Soff 1985; Drake 1988; Jentschura et al. 2005– obtained from the NIST Data base; remaining values are quoted from the supplemental fig. 4 in Tumlinson et al. 2017). Ionization energy is the energy required to ionize a species into its corresponding higher ion state (in this case, each of the five ions included in our analysis). Our ionization modelling is carried out with CLOUDYv17.

Ion	Wavelength (Å)	Ioniz. energy (eV)	log (T/K)	log ($n_{\rm H}$/cm^{-3})
H I	1216.00	13.6	4.0–4.5	∼2.0
Si III	1206.00	33.5	<5.0	−2.5
O VI	1031.00	138.12	5.5	−4.5
O VII	21.00	739.29	5.9	−5.0
O VIII	18.96	871.41	6.4	−5.5

more star-forming in comparison to the observations but this does not induce larger uncertainties in our analysis than already present due to multiple other factors which we highlighted earlier.

We also note that the SFR-averaged gas metallicity is consistent with the M31 measurement in Sanders et al. (2012).

2.2 Analysis

In this section, we describe the methodology adopted in order to compute the ion fractions in the CGM, underlying assumptions, their possible effects on the interpretation of our results and the process of creating Mollweide maps from the computed ion fractions. We make use of the photo-ionization code CLOUDY to obtain ionization fractions for the tracer ions H I, Si III, O VI, O VII, and O VIII, and we generate Mollweide projection maps using the HEALPY package to create mock observations.

2.2.1 Ionization modelling with CLOUDY

Two principal ionization processes in the CGM and IGM are collisional ionization and photo-ionization (Bergeron & Stasinska 1986; Prochaska et al. 2004; Turner et al. 2015). An equilibrium scenario is generally assumed in both these processes thus resulting in a collisional ionization equilibrium (CIE) and a photo-ionization equilibrium (PIE).

Such a bi-modal attempt in the ionization modelling has to date proved to be sufficient to well explain the co-habitation of both high and low ions in different phases at the same time within a common astrophysical gas environment. Generally, high ions (e.g. O VII, O VIII, Ne VIII, Mg X) are found to be better modelled via CIE, while the low and intermediate ions (e.g. Fe II, N I, S II) lend themselves better to PIE, owing to the temperatures in the various gas phases and the strength and shape of the UV background field. CIE, which assumes that the ionization is mainly carried by electrons, can be well characterized (Richter, Paerels & Kaastra 2008) using the relation,

$$f_{\rm H\ I,coll} = \frac{\alpha_{\rm H}(T)}{\beta_{\rm H}(T)}, \tag{1}$$

where $f_{\rm H\ I,coll}$ is the neutral hydrogen fraction in CIE, $\alpha_{\rm H}(T)$ is the temperature-dependent recombination rate of hydrogen and $\beta_{\rm H}(T)$ is the collisional ionization coefficient, both for hydrogen.

PIE, on the other hand, assumes photons to be the primary perpetrators and can be better described (Richter et al. 2008) as,

$$f_{\rm H\ I,photo} = \frac{n_{\rm e}\alpha_{\rm H}(T)}{\Gamma_{\rm H\ I}}, \tag{2}$$

where $f_{\rm H\ I,photo}$ is the neutral hydrogen fraction in PIE, $n_{\rm e}$ is the electron density, and $\Gamma_{\rm H\ I}$ is the photo-ionization rate.

We determine the ionization fractions using the CLOUDY code (version C17; Ferland et al. 2017), which is designed to model photo-ionization and photo-dissociation processes by including a wide combination of temperature–density phases for a list of elements, in order to simulate complex astrophysical environments realistically and produce mock parameters and outputs. The temperature of each AREPO gas cell is given as input to CLOUDY (in practice, we use lookup tables to speed up the calculation, see below), which determines the ionization state in post-processing. For the star-forming gas cell we directly set all atoms to be neutral, because most of the mass is in the cold phase.

We include both CIE and PIE in the modelling code. The UV background from Faucher-Giguère et al. (2009) is used. Self-shielding prescriptions, in particular for H I gas in denser regions, are adopted from Rahmati et al. (2013). We do not include AGN continuum radiation for the sake of simplicity. While excluding the AGN radiation might affect the ion fractions in regions close to the galaxy (e.g. ISM), it is much less likely to have any dominant impact in the CGM. Our CLOUDY modelling is identical to that introduced in Hani et al. (2018), with the only difference that we use a finer resolution grid for the output tables. In our analysis, we impose a metallicity floor of $10^{-4.5}$ $Z_{\odot}$ to avoid metallicity values lower than those present in our CLOUDY tables. Note that we do not include photo-ionization from stars or AGN in this work.

For this paper, we focus on the five tracer ions listed in Table 2 for which we generate mock observables; two of which are largely representative of the cold and cool-ionized ($T \sim 10^4 - 10^5$ K) gas (H I and Si III) and the three ions representative of the warm–hot ($T > 10^{5.5}$ K) gas (O VI, O VII, and O VIII). These five ions have a host of robust corresponding observational CGM data as well (e.g. Liang & Chen 2014; Werk et al. 2014; Johnson, Chen & Mulchaey 2015; Richter et al. 2016, 2017; Lehner et al. 2020).

Si III may also be produced by photoionization at a much lower temperature than 10^5 K. However, neither does our ionization modeling include photoionization from stars nor is it optimal in describing gas colder than 10^4 K. Therefore, this remains an uncertainty in our ionization modelling.

The overall ion abundances are naturally depending on the gas metallicity distribution in HESTIA. In Appendix A we therefore derive radial gas metallicity profiles for the simulated MW and M31 galaxies (see Fig. A1). We conclude that the disc gas metallicity in HESTIA is up to 3 times higher than realistic MW- and M31-mass galaxies (Sanders et al. 2012; Torrey et al. 2014). The gas metallicity profile of the CGM of MW and M31 is not well constrained observationally, but we speculate the HESTIA might as well have a slightly too high

gas metallicity there. We will keep this in mind when comparing our simulations to observations (see Section 3.5.3).

2.2.2 *Generation of skymaps*

The analysis in this paper extensively uses *skymaps* showing the column density distribution of the different ions. To define the unit vectors characterizing each sightline, we use the Mollweide projection functionality from the HEALPY package (Zonca et al. 2019), associated to the HEALPIX-scheme (Górski et al. 2005). Each HEALPIX sphere consists of a set of pixels (12 pixels in three rings around the poles and equator) that give rise to a *base resolution*. The grid resolution, $N_{\rm side}$, denotes the number of divisions along the side of each base-resolution pixel. The total number of equal-area ($\Omega_{\rm pix}$) pixels, $N_{\rm pix}$, can be expressed as, $N_{\rm pix} = 12N_{\rm side}^2$. The area of each pixel is, $\Omega_{\rm pix} = \pi/(3N_{\rm side}^2)$ and the angular resolution per pixel is, $\Theta_{\rm pix} = \Omega_{\rm pix}^{1/2}$. We select $N_{\rm side} = 40$ for all the Mollweide projection plots in this paper. This yields the total number of pixels (which we hereafter refer to as *sightlines*) $N_{\rm pix} = 19\,200$, and an angular resolution $\Theta_{\rm pix} = 1.46^\circ$.

Each sightline starts in $(x, y, z) = (0, 0, 0)$ (we shift our coordinates to our desired origin; see Section 3 for further discussion) and ends 700 kpc away in the direction of the unit vector defined by the HEALPix-pixel. A sightline is binned into 50 000 evenly spaced gridpoints, so we get a grid-size of 14 pc. At each gridpoint we set the ion density equal to the value of the nearest gas cell (we use the SCIPY-function, KDTree, to determine the nearest neighbour). The projected ion column density for a sightline is then calculated by summing the respective ion number densities over the grid-points constituting a sightline.

3 RESULTS

3.1 Skymaps

We create skymaps centred on the geometric centre of the LG, which we define to be the mid-point between MW and M31. Based on such skymaps we will later compute projected column density profiles of M31 (see Section 3.4), which makes it possible to directly compare our simulations to observations. A similar frame-of-reference also proved useful for Nuza et al. (2014), though they used it to obtain plots for studying the entire LG but did not produce whole skymaps from this point.

Fig. 1 shows Mollweide projections of the skymaps for each of the five ions – H I, Si III, O VI, O VII, and O VIII – for each LG realization (Table 1). All ions reveal an overdensity centred on the MW and M31. In this order, the ions trace gradually warmer gas, and it is therefore not surprising that we see a gradually more diffuse distribution in the projection maps. H I and Si III are much more centred on the inner parts of the haloes in comparison to O VI, O VII, and O VIII, the latter filling the space all the way out to R_{200} (and even beyond). R_{200} is shown as dashed circles around MW and M31 – note that a circle in a Mollweide projection appears deformed.

We see that all dense gas blobs with $N_{\rm H\,I} > 10^{20}$ cm^{-2} are associated with regions overlapping with the galaxies from our catalogue (see Appendix B). It fits well with the expectation that such high column densities are typically associated with the ISM of galaxies. The CGM regions of the MW and M31 analogues show a rich structure of H I-features. In 09–18, the M31 analogue, for example, reveals a bi-conical structure, characteristic of galaxy outflows. Many of the extended diffuse gas streams (particularly in Si III, but also in H I) go far beyond the haloes of the MW and M31 analogues. We see varying distributions of Si III gas across the three simulations in corresponding skymaps. While the 17–11 and 09–18 simulations show an excess of higher column density, clumpy Si III, 37–11 shows an excess of lower column density, diffuse Si III (See Sections 3.3.3 and 3.4 for further discussion). Smaller stellar mass and R_{200} values for MW–M31 in case of 37–11 (in comparison to the other two simulations) could be one possible reason for such a heterogeneity across the Si III distributions.

3.1.1 *Satellite galaxies in the LG*

The satellite galaxies in the simulations have been marked with a galaxy number in each panel, and their properties are summarized in the catalogue tables in Appendix B. We include those galaxies which have $M_{\rm gas} > 0$ (as identified by the SUBFIND halo finder) and are within 800 kpc of the LG centre. The 800 kpc cutoff is slightly larger in comparison to the 700 kpc cutoff, used when generating the skymaps; we have chosen this slightly larger cutoff for the satellite galaxy catalogue to ensure that all galaxies contributing to the skymaps are included. Below, we show that all dense H I blobs are associated with a galaxy from our catalogues, so a 800 kpc cutoff sufficiently selects all the galaxies contributing to the skymaps.

The satellite galaxies are generally more prominent in H I and Si III in comparison to the higher ions. Galaxy 12 from the 37–11 simulation does, however, reveal significant amounts of O VI, O VII, and O VIII. This satellite has a stellar mass of $M_* = 3.2 \times 10^9$ M$_\odot$, which is comparable to the LMC galaxy in the real LG (it has $M_* = 3 \times 10^9$ M$_\odot$ following D'Onghia & Fox 2016). Recently, it has been suggested that the LMC galaxy may have a warm–hot coronal halo (Wakker et al. 1998; Lucchini et al. 2020), which is responsible for the presence and spatial extent of the Magellanic Stream.

Adams, Giovanelli & Haynes (2013) presents a study of 59 ultra compact high-velocity clouds (UCHVCs) from the ALFALFA H I survey while Giovanelli et al. (2013) reports the discovery of a low-mass halo in the form of a UCHVC. From both these studies, a common conclusion emerges: low-mass gas-rich haloes (detected in the form of Compact HVCs/UCHVCs), lurking on the fringes of the CGMs of massive galaxies in our Local Volume (MW–M31, for example), are more likely to be discovered through their baryonic content (traceable primarily via H I). Other observational papers (de Heij, Braun & Burton 2002; Putman et al. 2002; Sternberg, McKee & Wolfire 2002; Maloney & Putman 2003; Westmeier, Braun & Thilker 2005b; Westmeier, Brüns & Kerp 2005a), based on objects detected around MW and M31, also support this hypothesis. We find similar H I column densities ($\sim 10^{19}$ cm^{-2}) at $R_{\rm proj} \lesssim R_{200}$ ($\lesssim$200 kpc), as reported in the above observations. One can also very clearly notice the presence of such small haloes in our skymaps. Hence, we can safely conclude that our results also support the existence of low-mass haloes at circumgalactic distances.

3.1.2 *Ram pressure stripping in the LG*

Many of the satellite systems show *disturbed* H I and Si III gas distributions (see the satellite galaxies with galaxy numbers 4 and 13 for simulation 09–18; 2, 5, and 7 for simulation 17–11; 2 for simulation 37–11) to varying degrees. The satellite galaxies' proximity to either of MW or M31 certainly plays a pivotal role (as do their own kinematic motions through their surroundings) in producing ram pressure stripping in their ISMs as well as generating asymmetries in their respective CGMs (Simpson et al. 2018; Hausammann, Revaz & Jablonka 2019). The ions tracing the warmer gas appear to be less sensitive to such disturbances.

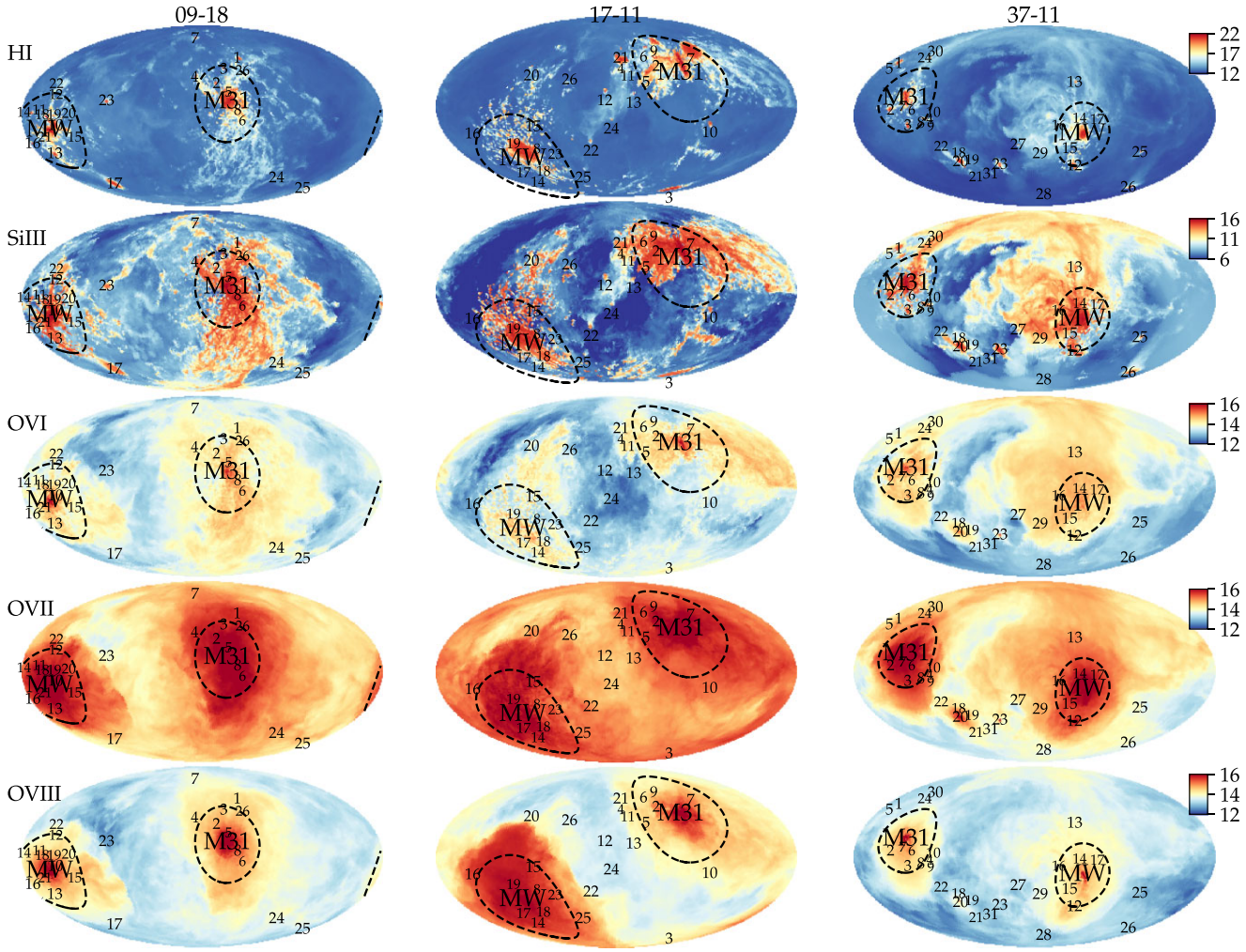

Figure 1. Skymaps showing the gas column densities in our three LG realizations. The maps are generated from an observer located in the LG centre, so we can see the predictions for both MW and M31 simultaneously. H I and Si III trace cold-dense gas in and around the ISM, whereas O VI, O VII, and O VIII trace gradually more hot-diffuse halo gas. Colour-bars show the log column densities, N, for each ion (N in units of cm^{-2}). Dashed lines indicate R_{200} of MW and M31. Small numbers indicate the location of galaxies other than M31 and MW. All dense H I absorbers with $N_{\rm H\,I} > 10^{20}$ cm^{-2} are associated with a galaxy. The distributions of the oxygen ions tracing warmer gas reveal a less clumpy and more spherical distribution around the massive galaxies.

In the context of galaxy clusters, ram-pressure stripping of the ISM gas is an important process in quenching galaxies (Gunn & Gott 1972; Abadi, Moore & Bower 1999). *Jellyfish galaxies* are examples of galaxies experiencing such stripping, where the ram-pressure from intracluster gas strips and disturbs the ISM of star-forming galaxies (Poggianti et al. 2017; Cramer et al. 2019). Such galaxies have long extended tails, which are stabilized by radiative cooling and a magnetic field (Müller et al. 2020). Given the many disturbed galaxies with extended tails in our simulations, we argue that observations of such galaxies may provide insights into the same processes, which are usually studied in jellyfish galaxies in galaxy clusters. It would specifically be interesting, if such examples of jellyfish galaxies in the LG could be used to provide insights into the growth of dense gas in the galaxy tails. The growth of dense gas in such a multiphase medium has recently been intensively studied in hydrodynamical simulations of a cold cloud interacting with a hot wind (Gronke & Oh 2018; Li, Bryan & Quataert 2019; Sparre, Pfrommer & Ehlert 2020; Kanjilal, Dutta & Sharma 2021; Abruzzo, Bryan & Fielding 2022). We further discuss the possibility of constraining gas flows in the tails of LG satellites in Section 4.

3.2 Cartesian projections

The inescapable nature of skymap projections often teases one into a likely misinterpretation of the angular extent spanned by objects within them. This misinterpretation, however, is circumvented by Cartesian projection plots. An example for this is the case of satellite galaxy number 7 in the 17–11 realization. Its distance to the LG mid-point is only 114 kpc (see Table B2 in Appendix B), which is much smaller in comparison to M31 (338 kpc). In the H I skymap, this galaxy appears much larger in comparison to the Cartesian projection, which we present in Fig. 2. This galaxy, hence, appears to be visually dominant in the Mollweide projection map simply because of its proximity to the LG centre, and its location on the skymap, where it appears to be in the direction of the M31 analogue. Thus, this example demonstrates that it is much harder to distinguish galaxies in the skymap in comparison to a Cartesian projection, which should be kept in mind when it comes to the visual interpretation of the skymaps.

In our analysis, all large and dense H I blobs with $N_{\rm H\,I} > 10^{20}$ cm^{-2} are associated with a galaxy from our galaxy catalogue. There is a

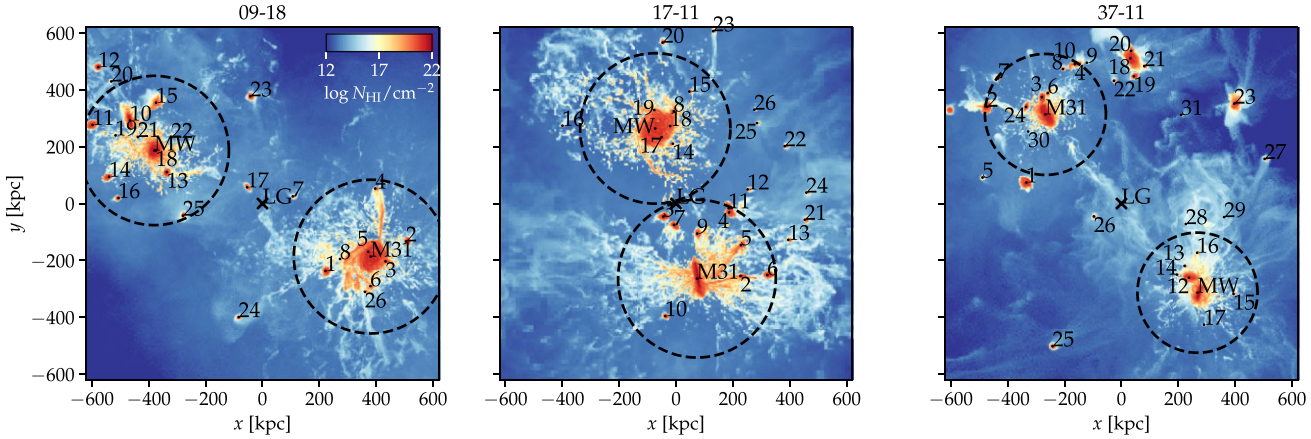

Figure 2. H I column density projection maps for each realization. The colour-bar denotes the range of log H I column densities (N in units of cm^{-2}). The dashed circles indicate R_{200} of M31 and MW. Note that the actual spatial extent spanned by galaxy number 7 in the 17–11 realization is far smaller as compared to its projected spatial extent in the corresponding skymap (Fig. 1; see also Section 3.2).

minor blob at $x < -600$ kpc in the 37–11 H I projection map (Fig. 2), which is not included in the catalogue, because its distance to the LG centre is larger than our cutoff value of 800 kpc – hence, it is not present in the skymaps, but only visible in the Cartesian projection.

We also see that the satellite galaxies, which we described in Section 3.1 as having *disturbed* gas distributions according to the skymaps, also look disturbed in Fig. 2. Indeed, the deformed nature seems even more pronounced in the Cartesian projection.

3.3 Power spectra

In the previous subsections, we have clearly seen that the low ions largely follow a clumpy distribution, while the high ions follow a much smoother profile. One way to neatly quantify such distribution patterns is by creating power spectra for each ion and capture the scales over which the corresponding ion exhibits most of its power.

3.3.1 Formalism

The spatial scales contributing to a skymap can be quantified by a power spectrum. First, the column density of a given ion is decomposed into spherical harmonics as

$$N_{\rm ion}(\boldsymbol{r}) = \sum_{lm} a_{lm} Y_l^m(\boldsymbol{r}), \tag{3}$$

where $\boldsymbol{r}$ is a pixels unit vector, l is the multipole number, and a_{lm} is the coefficient describing the contribution by the mode corresponding to a spherical harmonics base function (Y_l^m). The angular power spectrum is then defined as,

$$C_l = \frac{1}{2l+1} \sum_m |a_{lm}|^2. \tag{4}$$

We use the HEALPY function *anafast* to compute C_l for each of the column density skymaps. We have subtracted the monopole and dipole moments, and we constrain the power spectrum to $l \leq 2N_{\rm side} = 80$, because contributions at higher l may be dominated by noise (following the HEALPIX documentation for the anafast function).

In Fig. 3, we show the power spectra for the different ions. We show the power relative to $l = 2$, which makes the l-dependence for the different ions easy to compare. We have scaled the C_l by a factor of $l(l+1)$, so the plot shows the total power contributed by each multipole. The angular scale corresponding to each multipole number is estimated as $180^\circ/l$.

3.3.2 Contributions from odd and even modes

We start by characterizing the 09–18 simulation. The modes with even l-values are systematically larger in comparison to the modes with odd l-values. This *zigzagging* could easily be misinterpreted as an effect of noise, but we remark that it has a physical origin caused by the MW and M31 having a similar angular extent, a similar column density and being located in opposite directions (as seen from the skymap-observer's position). These two galaxies, hence, contribute with an approximate reflection-symmetric signal. Due to the identity, $Y_l^m(-\boldsymbol{r}) = (-1)^l Y_l^m(\boldsymbol{r})$, only the modes with even l contribute to a reflection-symmetric map, so this explains the domination of even modes.

A domination of even modes is especially visible for $l \lesssim 10$ for all ions in all three simulations. For 09–18 the domination is also present for higher l for all ions, but for 17–11, the signal vanishes at $l \gtrsim 10$ for O VI and O VII.

3.3.3 The angular coherence scale

From the behaviour of the power spectra for 09–18, we see that the H I skymaps have more structure on small scales of $\simeq 5^\circ$ (relative to a larger scale of $l = 2$) in comparison to the other ions. The amount of power on this angular scale ($\simeq 5^\circ$) is indeed gradually decreasing from H I, Si III, O VI, O VII to O VIII (with the only exception being O VIII in 37–11, which shows higher power on this scale than O VI and O VII). This is completely consistent with the picture that we get from visually examining the different skymaps in Fig. 1, where the ions tracing the coldest gas also seem to have the clumpiest distribution on small angular scales.

The behaviour of the power spectra for 17–11 and 37–11 are broadly consistent with this picture. H I has more power at smaller scales ($l \gtrsim 20$) across all simulations in comparison to the other four ions. For 37–11, O VIII shows more power on small scales in comparison to O VI and O VII, which is most likely an effect of the O VIII ion being influenced by outflows (this ion, for example, reveals a bi-conical outflow for MW for 37–11 in Fig. 1).

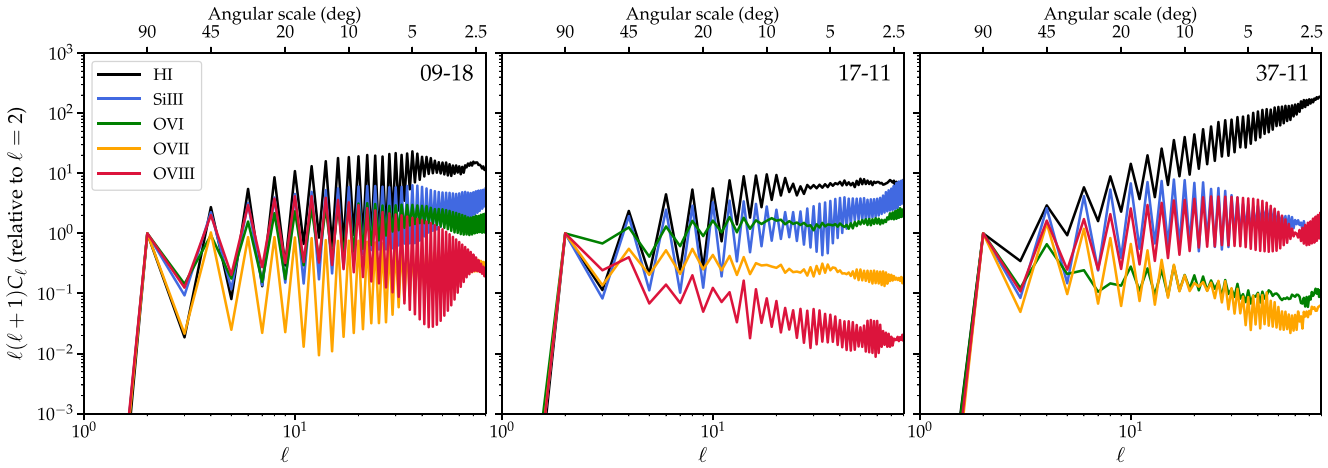

Figure 3. We show power spectra generated based on the ion skymaps (Fig. 1). The power spectra are normalized to the $l = 2$ value. The ions tracing the coldest gas (H I and Si III) have more power on small angular scales ($\lesssim 10^{\circ}$) in comparison to the high ions O VI, O VII, and O VIII. This fits well with the visual impression from the skymaps in Fig. 1. The power spectra reveal a preference for modes with even *l*-values. This is because the skymaps have a contribution from a reflective component, with MW and M31 being in opposite directions (as seen from the frame-of-reference of the skymap's observer).

For 37–11, the H I spectrum reveals the most power on small angular scales – this fits well with our scenario that H I gas is clumpy on small scales. For the warmer ions such as O VII the power is a decreasing function of *l* (if we ignore the fluctuations caused by even modes having more power in comparison to odd modes), implying that fluctuations on large angular scales are dominating. Similar trends are found in the other simulations.

Intriguingly, the Si III power spectra for 09–18 and 17–11 show an *increasing* trend at small scales ($\lesssim 10^{\circ}$), while 37–11 Si III power spectra shows a *decreasing* trend at similar scales. This pattern is, indeed, coherent with our observations regarding the Si III skymaps (see Section 3.1). We discuss this aspect a bit further in Section 3.4, where we introduce the column density distributions.

3.4 Column density profiles

Radial column density profiles are often used as an observational probe of the spatial distribution of the CGM in galaxies. In Fig. 4, we show the M31 radial profiles for our ensemble of ions with a particular focus on the median and 16–84th percentile of the distributions. The background points show all our sightlines.

3.4.1 Overall trends

As expected, the median column density is a declining function of radius for all ions in all simulations. The scatter is, however, behaving differently. Ions tracing the warm–hot gas (O VI, O VII, and O VIII) have a much lower scatter in comparison to the ions characteristic of dense–cold gas (H I and Si III). The profiles of the former ions are *well behaved* and the column density profiles can be well described as a monotonic decreasing function of projected distance (this feature is well documented for O VI; Werk et al. 2013; Liang, Kravtsov & Agertz 2018) with a scatter of 0.1–0.2 dex. On the other hand, H I and Si III reveal extreme outliers. In simulation 17–11 galaxies 4, 11, and 21 (see Fig. 1), for example, contribute with high H I column densities ($\gtrsim 10^{20}$ cm^{-2}) at a projected radius of $R_{\rm proj} = 1.5 \pm 0.5 R_{200}$. This shows that the H I column density is clumpy and influenced by satellite galaxies.

Similarly, Si III show multiple clumps, but their correlation scales seem slightly larger in comparison to H I, which is consistent with our power spectrum analysis. Despite the clumpy nature of Si III, we still find the mean of the projected column density profile to be decreasing (as, for example, is also seen in the observed sample of galaxies from Liang & Chen 2014).

These trends are also applicable to the projected column density profiles of the MW, which we show in the Appendix Fig. C1. H I is again influenced by individual satellite galaxies, and there is generally an increased scatter for ions tracing low-temperature gas in comparison to the high ions.

3.4.2 Origins of the clumpy CGM at large radii

The presence of H I sightlines mimicking Lyman limit-like column densities ($\sim 10^{17}$ cm^{-2}) in Fig. 4 as well as Si III sightlines lying above $\gtrsim 10^{12}$ cm^{-2}, out to R_{200} in our simulations, indicate that the cool-clumpy CGM extends to large distances up to virial radii. In fact, using VLT/UVES and *HST*/STIS data, Richter, Sembach & Howk (2003) as well as Richter et al. (2009) have identified such a population of Lyman-limit like optical and UV absorption systems in the Milky Way halo at high radial velocities, most likely representing the observational counterpart of CGM clumps far away from the disc. It is then worthwhile to contemplate about the physical origins of this clumpy CGM gas. A comparison with corresponding H I data from Liang & Chen (2014; henceforth, LC2014) reveals that the cool clumpy CGM ($\log N$(H I) $> 10^{16}$ cm^{-2}) has a similar spatial extent (> 2–$3\ R_{\rm proj}/R_{200}$) as seen in our data.

It is important to note that most of this clumpy CGM gas is not associated with the ISM of the satellite galaxies because those regions have far greater densities (a factor of $\sim$4–5 times higher) than that being discussed here. However, ram pressure stripping from the motions of many of the satellite galaxies within the R_{200} of MW–M31 can deposit such intermediate-column density cool gas at these distances. We elaborate on ram pressure stripping and its effects on the CGM of LG in Section 4.2.

Gas accretion mechanisms on to the host galaxy, in itself could be a potential source for cool, slightly underdense gas clumps manifesting as cold CGM at large distances.

Galactic fountain flows have long been hypothesized as a possible means to efficiently circulate gas, metals, and angular momentum between the ISM and the CGM (Fraternali et al. 2013; Fraternali

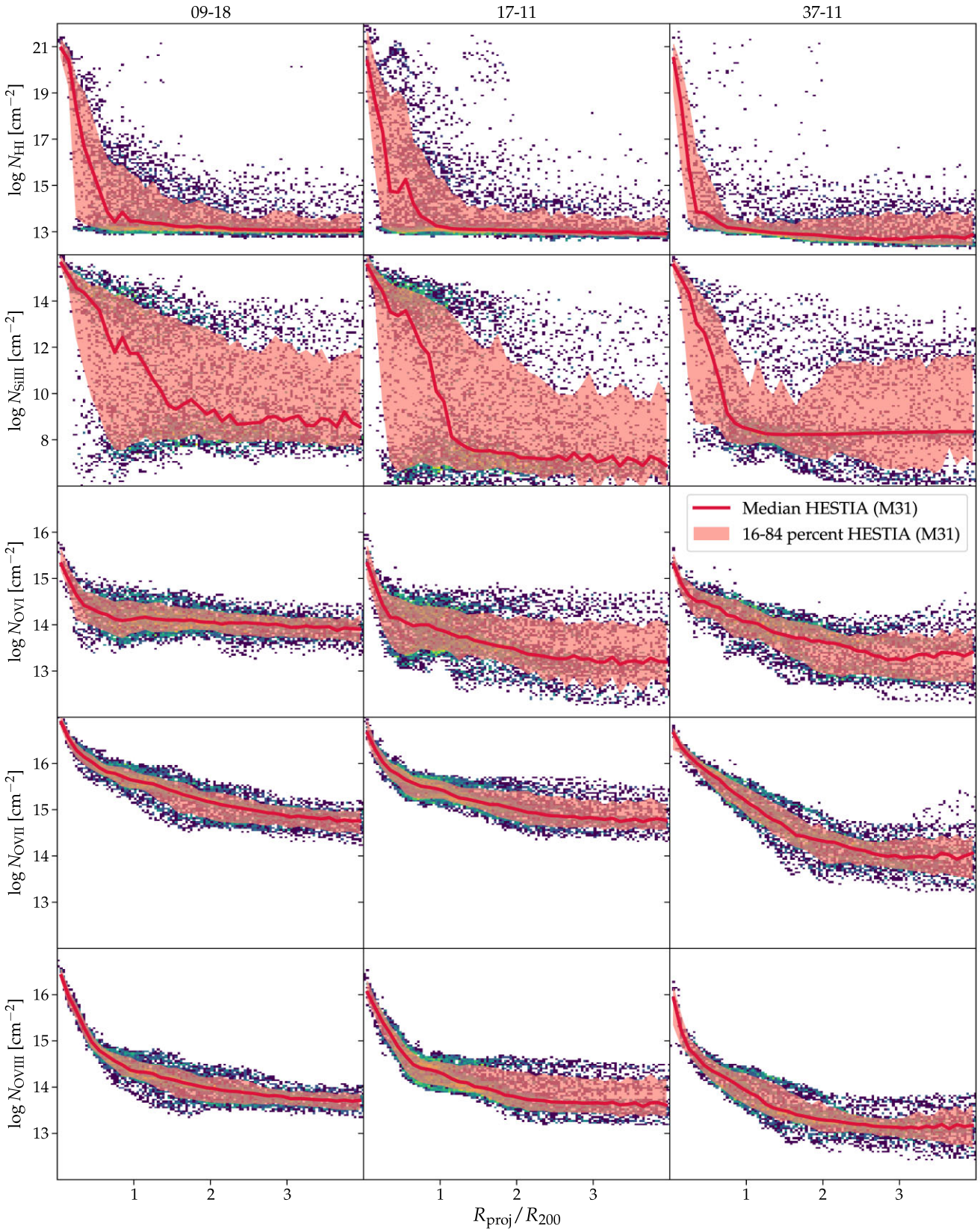

Figure 4. *Top-Bottom*: 2D log radial column density profiles for M31 for H I, Si III, O VI, O VII, and O VIII. Thick red curve signifies median values, while the red shaded region denotes 16–84th percentile values. The background points depict the ion column density contributions arising from the remaining gas cells. A distinct blob of high column density H I absorbers, which can be seen at a distance of $\sim$1.5 R_{proj}/R_{200} in the H I profile for 17–11, can be correlated with satellite galaxies numbered 4 and 11 in the corresponding skymap (H I skymap for 17–11 in Fig. 1).

2017). Thermal instabilities arising from cold gas parcels from the ISM regions moving outward rapidly through the warm ambient CGM regions can result in the growth of intermediately dense cool gas. However, it is not immediately clear which of the above three processes could be the most dominant. While carrying out an elaborate tracer particle analysis or delving deeper into the ram pressure stripping processes could provide better clarity about the root cause of this distant cold CGM, it is beyond the scope of this paper.

3.4.3 *The bi-modal distribution of Si III*

Interestingly, Si III column density distributions show a strong bi-modality, with a higher sequence of sightlines clustered around $\sim 10^{14}$ cm^{-2} and another lower sequence clustered around $\sim 10^{8}$ cm^{-2}. This bimodality is expected due to the bi-conical outflows, which we identified in Fig. 1. This bimodal feature is indeed most prevalent for M31 in 09–18 and 17–11, where the bi-conical outflows were most visible. However, it is practically highly unlikely to detect the lower sequence of Si III column densities in near future; hence, this bi-modal feature will not show up in the Si III observational data sets.

3.5 Comparison with observations

While the previous subsections primarily dealt with the theoretical interpretations of our results from the power spectra and column density profiles, this subsection is dedicated to analysing how well these results match with data from observations and other simulations. We base our comparison on three different observational data sets:

(i) **M31 observations from the Project AMIGA** (Absorption Maps in the Gas of Andromeda; Lehner et al. 2020). Project AMIGA is a UV *HST* program studying the CGM of M31 by using 43 quasar sightlines, piercing through its CGM at different impact parameters ($R_{\rm proj}$ = 25 to 569 kpc). Such a large number of sightlines for the Andromeda galaxy enables a constraining quantitative comparison to the corresponding mock data from our simulations.

(ii) **Absorption-line measurements of Si III from LC2014**. They present a study of low and intermediate ions in the CGMs of a sample of 195 galaxies in the low-redshift regime. However, 50 per cent of the LC2014 sample consists of dwarf galaxies. To enable a fair comparison, we select only galaxies in a comparable mass range to our M31 simulations. We specifically only include their galaxies with $10^{10.6}\,{\rm M}_{\odot} \leq M_{*} \leq 10^{11.1}\,{\rm M}_{\odot}$. In our context, the data pertaining to Si III (1206 Å) ion is relevant. Since this is an absorption-line study, they measure all ion abundances in terms of equivalent width (EW). In order to translate their EW measurements into column density values, we plot a corresponding curve of growth for different '*b*' parameters. From the curve of growth it is clear that for $\log N({\rm Si\,III}) < 12.0$ and $\log N({\rm Si\,III}) > 18.0$, translating EW into column densities is straightforward. However, in the $12.0 < \log N({\rm Si\,III}) < 18.0$ regime, *b*-parameter degeneracy sets in and a single EW measurement can result in different values for column densities depending on the *b*-parameter adopted. For this reason we exclude the sightlines from LC2014 at distances $d/R_{200} < 1$ (where this degeneracy is present).

(iii) **O VI ion measurements from Johnson et al. (2015; henceforth J2015)**. They present a study of distribution of heavy elements of sighlines passing galaxies with different impact parameters. Like LC2014, the eCGM galaxy sample in J2015 also comprises of galaxies spanning a range of stellar masses ($\log {\rm M}_{*}/{\rm M}_{\odot} = 8.4$–$11.5$), so we again apply a mass cut of $10^{10.6}\,{\rm M}_{\odot} \leq M_{*} \leq 10^{11.1}\,{\rm M}_{\odot}$ and we also only include late-type galaxies.

In Fig. 5 we compare the projected Si III and O VI profiles for M31 from HESTIA to these observational data sets, and we also show the EAGLE simulations (Oppenheimer et al. 2017) and the FIRE-2 simulations (Ji et al. 2020). We discuss the comparison to the other simulations in Section 3.6.

3.5.1 *Comparing HESTIA to Si III observations*

At low impact parameters, $R_{\rm proj} \lesssim R_{200}$, the observed range of Si III column densities in AMIGA and our simulations are consistent.[2] For sightlines probing $R_{\rm proj} \gtrsim 1.5R_{200}$, our simulations underpredict the observed column densities. Some of the shown observational data points are upper limits, implying that the observations leave the possibility for individual sightlines with column densities as low as ours, but the simulations generally fall short by at least an order of magnitude at $R_{\rm proj} \gtrsim 1.5R_{200}$.

On the other hand, HESTIA is perfectly consistent with the upper limits from LC2014. Indeed, there are tensions between the high Si III column densities reported by Project AMIGA (in M31) and the upper limits from LC2014. A possible reason for this could be contamination of gas from the MW halo or LG environment for the M31 observations. We will further assess this hypothesis in Section 4.1.

3.5.2 *Comparing HESTIA to O VI observations*

When comparing the O VI column density in AMIGA and HESTIA we again see larger values in the former. At the same time, HESTIA reveals larger column densities in comparison to the J2015 observations of galaxies from the low-redshift Universe.

The offset between the observed J2015 and AMIGA might again be caused by contamination of MW absorption in the latter data set, or an alternative possibility for the offset is that one data set is the mean of a sample of low-redshift galaxies and the other only takes into account a single galaxy's profile (M31).

3.5.3 *The normalization of the metallicity profile in HESTIA*

In Appendix A we show that the gas metallicity in the disc of the HESTIA galaxies is up to a factor of 3 higher in comparison to observations. The naïve expectation is that the CGM gas metallicity is too high by a similar factor, and this would cause the HESTIA column density profiles in Fig. 5 to be overestimated by up to 0.5 dex. If we scale the HESTIA M31 Si III and O VI column density profiles down by 0.5 dex, the agreement with LC14 and J2015 improves, whereas the tension between the AMIGA observations and HESTIA becomes stronger. This supports our conclusion that HESTIA is well consistent with these observations of low-redshift galaxies.

3.6 Comparison with other simulations

Fig. 5 also shows the profiles for Si III and O VI for EAGLE-based (Oppenheimer et al. 2017) and FIRE-2 (Ji et al. 2020) based simulation data sets. For the comparison with EAGLE, we use the Si III and O VI profiles from their $L_{\star}$ subsample, which has $\log M_{200} = 11.7$–$12.3\,{\rm M}_{\odot}$. It contains 10 haloes hosting star-forming galaxies. These are zoom simulations with non-equilibrium cooling. The

[2]This is, of course, keeping in mind the uncertainties associated with the ion column densities in the innermost regions of the galaxies in our simulations, i.e. regions where the ISM is dominant.

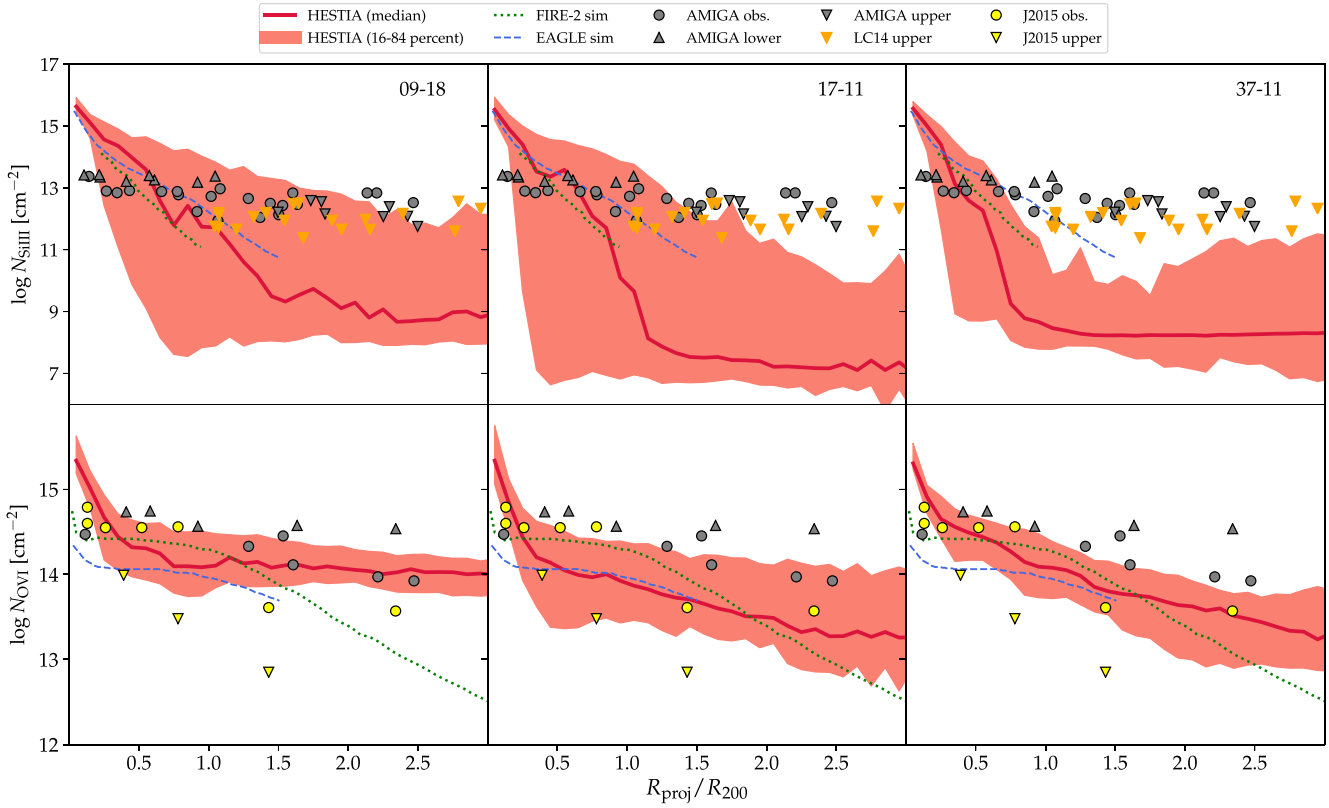

Figure 5. The top (bottom) panel shows the Si III (O VI) radial column density profiles for our three realizations for M31. The thick red curve denotes the median values while the red shaded region denotes the 16–84th percentiles for our realizations. Circles refer to the detections while the downward and upward triangles, respectively, denote the upper and lower limits in the Project AMIGA survey (Lehner et al. 2020). The blue dashed line denotes the data from EAGLE simulations (Oppenheimer et al. 2017), while the green dash–dotted line denotes the data from FIRE-2 simulations (Ji et al. 2020). Downward orange triangles in the upper panel are Si III upper limits from the Liang & Chen (2014), while the yellow filled circles and downward triangles in the lower panel are O VI measurements from Johnson et al. (2015). The Si III profile from HESTIA is consistent with the LC14 upper limits, but there is an inconsistency between these and the Project AMIGA observations. Similarly, the J2015 and Project AMIGA observations of O VI are inconsistent, and HESTIA is only in reasonable agreement with J2015. In Fig. 6 we discuss that a likely explanation for the offset between HESTIA and the AMIGA observations is contamination of gas from the MW to the AMIGA data set.

corresponding average R_{200} for this subsample is $\simeq$ 195 kpc (see fig. 2 in Oppenheimer et al. 2016). This data set is at $z = 0.2$, since the authors compare it with the COS-Halos data which covers the same redshift. For the FIRE-2 simulation comparison we compare to the m12i halo ($\log M_{200} \simeq 12$ M$_\odot$ at $z = 0$) using the FIRE-2 model with cosmic ray feedback (their simulation data is taken from fig. 17 in Lehner et al. 2020). Further details about the simulations and CGM modelling in FIRE2 simulations can be found in Ji et al. (2020).

The HESTIA simulations show many similar trends to EAGLE and FIRE-2 and they, furthermore, *all* underpredict the AMIGA column densities of Si III and O VI at $R_{\rm proj} \gtrsim 1.0R_{200}$. On the other hand, all the simulations are broadly consistent with the observational data sets we have compiled based on LC2014 and J2015.

3.7 Convergence test

In Appendix D we compare the high-resolution HESTIA simulations analysed in Fig. 5 with intermediate-resolution simulations having an eight times larger dark matter particle mass. This convergence test does not challenge our derived column density profile.

Using the same simulation code and galaxy formation model as in our paper, van de Voort et al. (2019) showed that increasing the spatial resolution significantly boosts the H I column density in the CGM. Idealized simulations furthermore reveal the possibility of gas to fragment to the cooling scales (McCourt et al. 2018; Sparre, Pfrommer & Vogelsberger 2019), which for dense gas is significantly below our resolution limit. Exploring the resolution requirement in the CGM of cosmological simulations is, however, still a field of ongoing research, so it is still a possibility that the idealized simulations overestimate the needed spatial resolution.

We note that Si III and O VI trace warmer gas in comparison to H I, so these ions are expected to be less affected by resolution issues than H I. Even though our convergence test does not reveal any signs of a lack of convergence, it is still a possibility that our column densities are affected by a too low spatial resolution.

4 DISCUSSION

4.1 Biased column density profiles caused by the MW's CGM?

We have found that observations of low-redshift galaxies disagree with the observed column densities of the M31 by the Project AMIGA. A possible explanation for this finding could be observational biases, for example, caused by gas clouds in the CGM of the MW contributing to the projected column density profile of M31. Such a bias does not play a role in our previous skymap analysis, because the skymaps are created by an observer in the geometric

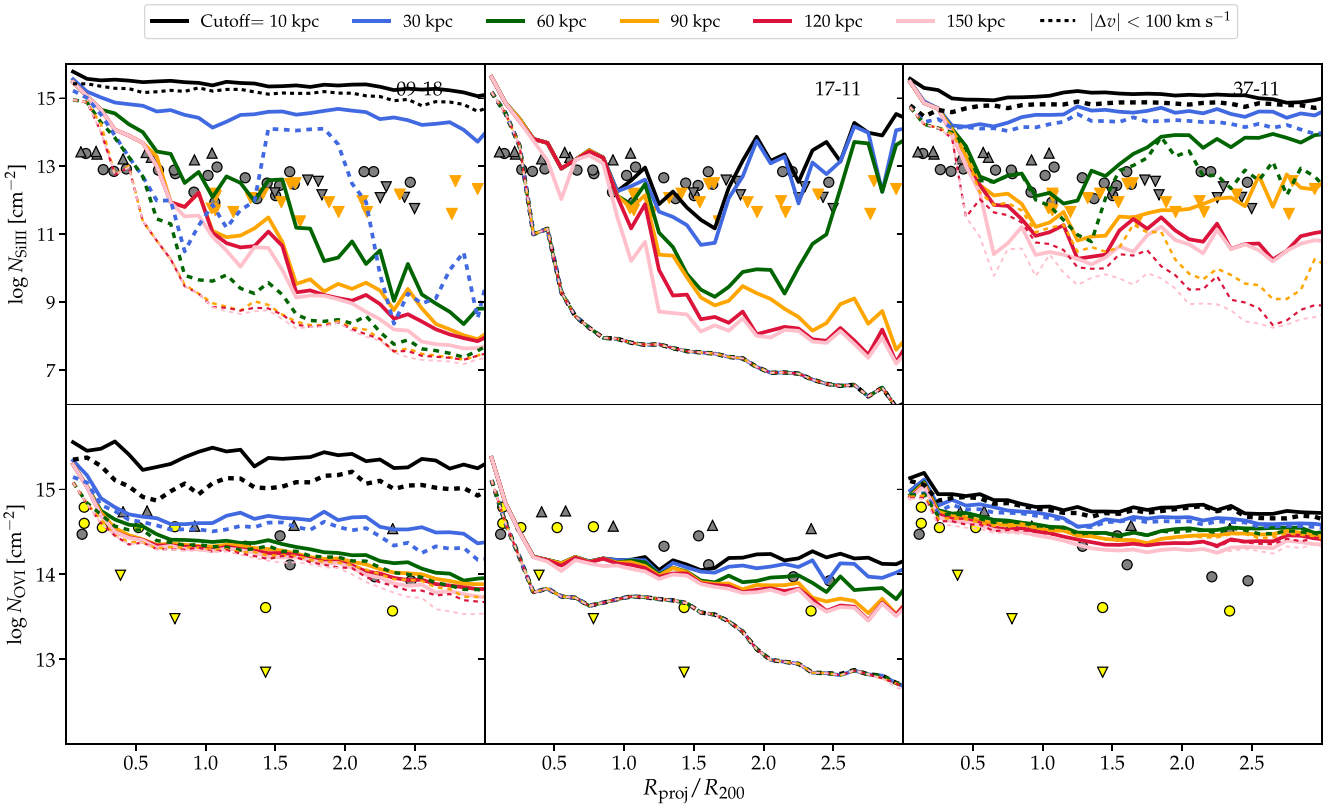

Figure 6. We demonstrate how the gas in the MW's CGM may influence the observationally derived median column density profiles around M31. We have generated skymaps centred on the MW (instead of the LG, as done in previous figures), where we remove gas lying within a radial cutoff ranging from 10 to 150 kpc from MW (solid lines). For the dashed lines we additionally constrain gas to be within 100 km s^{-1} of the M31. As in Fig. 5, the data points from Project AMIGA survey (filled grey markers), LC2014 (orange downward markers), and J2015 (filled yellow markers) have been overplotted. Even when only including gas within 100 km s^{-1} of M31, the Si III profile of 09–18 and 37–11 is increased to $\simeq 10^{15}$ cm^{-2} by clouds within 10–120 kpc from the MW centre. For 17–11, a velocity selection of gas very well removes gas within 150 kpc of the MW. For O VI, the contamination from the MW's CGM is also significantly changing the profiles in 09–18 – here gas residing within 150 kpc of the MW may boost the column density by 1.0 dex.

centre of the LG, and hence, the MW's CGM does not contribute to the sightlines towards M31.

We now turn to addressing the role of such a bias in the three realizations of the HESTIA simulations. We re-analyse our simulations with an observer located in the MW centre, and create skymaps of the different ions as before. In order to incorporate the larger distance from the MW to M31 (as opposed to the smaller distance from the LG centre to M31 in earlier analysis), we use longer sightlines (each 1400 kpc in length). To ensure grid-size uniformity with respect to the earlier analysis, we increase the number of gridpoints from 50 000 to 100 000. To determine the role of the MW's CGM, we create skymaps excluding gas within 10, 30, 60, 90, 120, and 150 kpc of the MW's centre. The corresponding projected radial column density profiles are seen as solid lines in Fig. 6. The three different realizations show a significant amount of Si III and O VI residing in the MW's CGM at a distance of 10–120 kpc from the MW's centre.

Observationally, a hint of the gas clouds' spatial origin can be obtained by looking at its line-of-sight velocity. In Fig. 6 we also construct profiles, where we exclude gas clouds with a line-of-sight difference ($|\Delta v|$) exceeding 100 km s^{-1} from M31's velocity (see dashed lines in Fig. 6). From our different realizations we see a different behaviour. For 09–18 and 37–11, the column density profiles of Si III and O VI increase up to 10^{15} cm^{-2} and by 1.0 dex, respectively (this is the difference between dashed lines indicating a cutoff of 10 kpc and 120 kpc in Fig. 6), caused by gas residing between 10 and 120 kpc of the MW's CGM. For 17–11, the situation is less extreme, and the inferred column density profile of M31 is unaffected by the MW, when a velocity cut in the line-of-sight velocity is applied.

This analysis shows that the MW's CGM can substantially bias the inferred projected column densities of M31. For Si III, the potential bias is stronger in comparison to O VI. For O VI in 17–11, a velocity cut alone is successful in completely removing MW contributions. As seen from the lower middle panel in Fig. 6, this still gives us a small discrepancy (∼0.5 dex) with AMIGA observations. This means that our 17–11 analogues inherently do not produce enough O VI to completely match the AMIGA observational trends. However, the opposite is true for the other two simulations where we clearly see our results matching fairly well with the AMIGA observations, when we include the contribution of gas from the MW halo. Overall, we infer that the biases estimated by our MW centred skymaps provide a likely explanation for the differences between the HESTIA simulations and the AMIGA observations (seen in Fig. 5). At the same time, it also provides a likely explanation for the differences between the low-redshift galaxy samples (LC2014 and J2015) and the Project AMIGA.[3]

[3]However, we do note here that both LC2014 and J2015 are a representative sample as opposed to the Project AMIGA observations, which pertain to a single galaxy.

In reality, contamination of the gas from the Magellanic Stream (MS) to the M31 CGM observations is also a possibility. The MS passes just outside of the virial radius ($R_{\rm vir} = 300$ kpc) of M31 (see fig. 1 in Lehner et al. 2020). For the purpose of ascertaining the level of MS contamination, Lehner et al. (2020) use Si III as their choice of ion (mainly because it is most sensitive to detect both weak as well as strong absorption). However, they do not remove entire sightlines merely on the suspicion of possible MS contamination. Instead, they analyse individual components and find that 28 out of 74 (38 per cent) Si III components are within the MS boundary region (and having Si III column density values larger than 10^{13} cm^{-2}). These are not included in the sample from then on. For the remaining *non-MS contaminated* components, they find a trend of higher Si III column density at regions away ($b_{\rm MS} > 15^{\circ}$) from the MS main axis ($b_{\rm MS} = 0^{\circ}$). This shows that the MS contamination is negligible for these components.

However, they do find a fraction (4/22) of dwarf galaxies out of their M31 dwarf galaxies sample falling in the MS contaminated region. This means that while they do take utmost care to avoid any MS contamination in their results, there could still be some residual contributions (especially in the cold gas observations of M31's CGM) from the MW CGM. These could manifest in the form of slightly enhanced column densities in observations at regions beyond M31's virial radius.

4.2 Gas stripping in the Local Group

A characteristic that appears across all our realizations is the distorted nature of the CGMs of many satellite galaxies. High-velocity infall motions of dwarf galaxies through complex gravitational potential fields, typical in galaxy groups and clusters results in the dwarf galaxy CGM becoming structurally disturbed. In some extreme cases this can also result in trailing stripped gas tails (Smith et al. 2010; Owers et al. 2012; Salem et al. 2015; McPartland et al. 2016; Poggianti et al. 2017; Tonnesen & Bryan 2021). While a few very clear examples of such galaxies have been described in detail in Section 3.1, there are certainly many more.

The role of stripped gas from the CGMs of satellite galaxies towards augmenting the pre-existing gas reserves of the host galaxy and thereby influencing the CGM of the host galaxy is rather well known from the observations of the MS, which emanates from the interaction of the small and large magellanic clouds on their approach towards the MW (e.g. Fox et al. 2014; Richter et al. 2017). However, a scarcity of deep observations means that very little is known about the part played by the diffuse gas from other satellite galaxies in our LG. Few studies pertaining to such observations reveal low neutral gas abundances around dwarf galaxies, though they might still harbour sizeable reserves of ionized gas (Westmeier et al. 2015; Emerick et al. 2016; Fillingham et al. 2016; Simpson et al. 2018).

By carefully analysing the gas flow kinematics across time-frames for these dwarf galaxies within HESTIA, it will be possible, in future studies, to obtain not just their mock proper and bulk gas motions, but also various parameters regarding their stripped gas such as its spatial extent, cross-section, and physical state. The Gaia DR2 proper motions of MW and LG satellites (Pawlowski & Kroupa 2020), along with corresponding comprehensive UV, optical and X-ray data sets from *HST*-COS, UVES, Keck and Chandra, can then provide us with clues regarding which HESTIA realizations are most likely to produce these real observations. Furthermore, implementing similar sightline analysis, done in this paper for MW–M31, for multiple satellite systems over a range of their respective impact parameters, can yield extensive mock data sets that could then prove useful in the wake of future surveys that will be sensitive to even lower column density gas.

4.3 Physical modelling of the CGM

In recent years, our understanding of the CGM has dramatically improved, and it is encouraging that our simulations are broadly consistent with observations. This is despite of our relatively simple physics model.

Theoretical work has for example suggested that parsec-scale resolution, which is so far unattainable in cosmological simulations like HESTIA, may be necessary to resolve the cold gas in galaxies (McCourt et al. 2018; Hummels et al. 2019; Sparre et al. 2019; van de Voort et al. 2019, – we note, however, that these results are so far only suggestive and the need for parsec-scale resolution has so far not been demonstrated, yet this could be a potential reason for the offset). Results from van de Voort et al. (2019) proved that ∼1 kpc resolution in the CGM boosts small-scale cold gas structure as well as covering fractions of Lyman limit systems; this might also hold true for slightly less dense but slightly more ionized cool gas. McCourt et al. (2018) proposed a cascaded shattering process via which a large cloud experiencing thermal instability can cool a couple of orders of magnitude (from $T \sim 10^6$ K to $\sim 10^4$ K), mainly as a result of continued fragmentation within the larger cloud. They compute the characteristic length-scale, associated with shattering, to be ∼1–100 pc. Multiple observations also show that cool gas is indeed present in form of small clouds out to $\sim R_{\rm vir}$ in galaxy haloes (Prochaska & Hennawi 2008; Stocke et al. 2013; Hennawi et al. 2015; Lau, Prochaska & Hennawi 2016). Using Cloudy ionization models, Richter et al. (2009) have determined the characteristic sizes of the partly neutral CGM clumps in the MW halo based on their *HST*/STIS absorption survey, leading to typical scale lengths in the range 0.03 to 130 pc (see tables 4 and 5 in Richter et al. 2009). From their absorber statistics, these authors estimated that the haloes of MW-type galaxies contain millions to billions of such small-scale gas clumps and argue that these structures may represent transient features in a highly dynamical CGM. Thus, it is clear that the length-scales involved in these processes are still at least an order of magnitude below what is currently achievable in the highest resolution zoom-in simulations. It is also worth mentioning that Fielding & Bryan (2022) have recently introduced a novel framework modelling multiphase winds, which may be relevant for future cosmological simulations of the CGM.

Lehner et al. (2020) discusses feedback processes, which may also affect how gas and metals are transported to large radii. The role of cosmic ray feedback in influencing the CGM has recently gained interest from multiple research groups (Salem, Bryan & Hummels 2014; Salem, Bryan & Corlies 2016; Buck et al. 2020; Hopkins et al. 2020; Ji et al. 2020), and it has been shown to significantly alter gas flows in the CGM of simulations. CR-driven winds from the LMC (Bustard et al. 2020) as well as those from the resolved ISM (Simpson et al. 2016; Farber et al. 2018; Girichidis et al. 2018) have been shown to change both the outer and inner CGM properties, respectively. Similarly, magnetic fields have been shown to influence the physical properties of the CGMs of simulated galaxies, thereby modifying the metal-mixing in the CGM (van de Voort et al. 2021).

Despite of HESTIA agreeing relatively well with the observations, we note that there are still some important challenges for future galaxy formation models in terms of understanding physical processes in the CGM.

5 CONCLUSIONS

We have analysed the gas, spanning a range of temperatures and densities, around the MW–M31 analogues at $z = 0$ in a set of three HESTIA simulations. These LG simulations use the quasi-Lagrangian, moving mesh AREPO code, along with the comprehensive Auriga

galaxy formation model. We have set our frame of reference to the LG geometrical centre and generated ion maps for a set of five ions, H I, Si III, O VI, O VII, and O VIII. Some important conclusions have emerged from our study:

(i) We have created mock skymaps of the gas distribution in the LG. All dense gas blobs with $N_{\rm H\,I} > 10^{20}$ cm^{-2} are associated with a galaxy; either a satellite galaxy or MW/M31 themselves. The skymaps of H I and Si III reveal strong imprints of satellite galaxies, whereas the tracers of warmer gas (O VI, O VII, and O VIII) are mainly dominated by the haloes of MW and M31. The projected column density profiles of the latter ions are, indeed, well described by monotonic decreasing functions of the impact parameter. In comparison, the projected H I- and Si III-profiles have a much higher scatter caused by blobs associated with the satellite galaxies.

(ii) A power spectrum analysis of the skymaps shows that H I, Si III, O VI, O VII, and O VIII have a gradually higher coherence angle on the sky – ions tracing the coldest gas are most clumpy. This confirms the impression we get by visually inspecting the skymaps, and it is also consistent with the behaviour of the column density profiles.

(iii) The visual inspection of the simulated skymaps reveal multiple satellite galaxies with disturbed gas morphologies, especially in H I and Si III. These are LG analogues of jellyfish galaxies. Future simulation analyses and observations can give a unique insight to the physical processes in the ISM and CGM of these galaxies.

(iv) For the HESTIA M31 analogues we compare the Si III and O VI column density profiles to observations of M31 and low-redshift galaxies. The spectroscopic observations of M31 and low-redshift galaxies reveal remarkably different column density profiles. Using our simulations, we find that the gas residing in the Milky Way may contaminate the sightlines towards M31, such that the M31 column densities are boosted. For Si III and O VI we see this contamination boosting the column density profiles up to as much as 10^{15} cm^{-2} and by 1.0 dex, respectively, even when only including gas within a 100 km s^{-1} of the M31 velocity. Contamination of gas from the MW, hence, provides one of the likely explanations for the offset between observations of M31 and low-redshift galaxies.

(v) The M31 analogues from HESTIA have Si III and O VI column density profiles broadly consistent with low-redshift galaxy constraints. If we include a contamination from MW gas, then in 2 out of 3 M31 realizations we can also reproduce the large column densities observed in the direction of M31 in Project AMIGA.

ACKNOWLEDGEMENTS

We thank Moritz Itzerott, Martin Wendt, Gabor Worseck for useful comments and discussions. We also thank the anonymous referee for some very constructive comments which greatly improved the quality of this paper. MS acknowledges support by the European Research Council under ERC-CoG grant CRAGSMAN-646955. MHH acknowledges support from William and Caroline Herschel Postdoctoral Fellowship Fund. SEN is a member of the Carrera del Investigador Científico of CONICET. He acknowledges support by the Agencia Nacional de Promoción Científica y Tecnológica (ANPCyT, PICT-201-0667). RG acknowledges financial support from the Spanish Ministry of Science and Innovation (MICINN) through the Spanish State Research Agency, under the Severo Ochoa Program 2020-2023 (CEX2019-000920-S). MV acknowledges support through NASA ATP grants 16-ATP16-0167, 19-ATP19-0019, 19-ATP19-0020, 19-ATP19-0167, and NSF grants AST-1814053, AST-1814259, AST-1909831 and AST-2007355. ET acknowledges support by ETAg grant PRG1006 and by EU through the ERDF CoE grant TK133. The authors sincerely acknowledge the Gauss Centre for Supercomputing e.V. (https://www.gauss-centre.eu/) for providing computing time on the GCS Supercomputer SuperMUC at the Leibniz Supercomputing Centre (http://www.lrz.de/) for running the HESTIA simulations. We thank the contributors and developers to the software packages YT (Turk et al. 2011) and ASTROPY (Astropy Collaboration et al. 2018), which we have used for the analysis in this paper.

DATA AVAILABILITY

The scripts and plots for this article will be shared on reasonable request to the corresponding author. The AREPO code is publicly available (Weinberger, Springel & Pakmor 2020).

REFERENCES

Abadi M. G., Moore B., Bower R. G., 1999, MNRAS, 308, 947
Abruzzo M. W., Bryan G. L., Fielding D. B., 2022, ApJ, 925, 199
Adams E. A. K., Giovanelli R., Haynes M. P., 2013, ApJ, 768, 77
Agertz O., Kravtsov A. V., 2015, ApJ, 804, 18
Anglés-Alcázar D., Faucher-Giguère C.-A., Kereš D., Hopkins P. F., Quataert E., Murray N., 2017, MNRAS, 470, 4698
Angulo R. E., Springel V., White S. D. M., Jenkins A., Baugh C. M., Frenk C. S., 2012, MNRAS, 426, 2046
Appleby S., Davé R., Sorini D., Storey-Fisher K., Smith B., 2021, MNRAS, 507, 2383
Astropy Collaboration, 2018, AJ, 156, 123
Aumer M., White S. D. M., Naab T., Scannapieco C., 2013, MNRAS, 434, 3142
Bahcall J. N., Spitzer L., Jr, 1969, ApJ, 156, L63
Barmby P. et al., 2006, ApJ, 650, L45
Behroozi P. S., Conroy C., Wechsler R. H., 2010, ApJ, 717, 379
Behroozi P. S., Wechsler R. H., Conroy C., 2013, ApJ, 770, 57
Berg T. A. M., Ellison S. L., Tumlinson J., Oppenheimer B. D., Horton R., Bordoloi R., Schaye J., 2018, MNRAS, 478, 3890
Bergeron J., Stasinska G., 1986, A&A, 169, 1
Bish H. V., Werk J. K., Peek J., Zheng Y., Putman M., 2021, ApJ, 912, 8
Bland-Hawthorn J., Gerhard O., 2016, ARA&A, 54, 529
Boardman N. et al., 2020, MNRAS, 498, 4943
Bogdán Á. et al., 2013, ApJ, 772, 97
Boissier S., Prantzos N., 1999, MNRAS, 307, 857
Booth C. M., Schaye J., 2009, MNRAS, 398, 53
Bordoloi R. et al., 2014, ApJ, 796, 136
Borthakur S., Heckman T., Strickland D., Wild V., Schiminovich D., 2013, ApJ, 768, 18
Buck T., Pfrommer C., Pakmor R., Grand R. J. J., Springel V., 2020, MNRAS, 497, 1712
Bustard C., Zweibel E. G., D'Onghia E., Gallagher J. S. I., Farber R., 2020, ApJ, 893, 29
Carlesi E. et al., 2016, MNRAS, 458, 900
Ceverino D., Dekel A., Bournaud F., 2010, MNRAS, 404, 2151
Chomiuk L., Povich M. S., 2011, AJ, 142, 197
Conroy C., Naidu R. P., Zaritsky D., Bonaca A., Cargile P., Johnson B. D., Caldwell N., 2019, ApJ, 887, 237
Cramer W. J., Kenney J. D. P., Sun M., Crowl H., Yagi M., Jáchym P., Roediger E., Waldron W., 2019, ApJ, 870, 63
Creasey P., Scannapieco C., Nuza S. E., Yepes G., Gottlöber S., Steinmetz M., 2015, ApJ, 800, L4
D'Onghia E., Fox A. J., 2016, ARA&A, 54, 363
Das S., Mathur S., Nicastro F., Krongold Y., 2019a, ApJ, 882, L23
Das S., Mathur S., Gupta A., Nicastro F., Krongold Y., Null C., 2019b, ApJ, 885, 108
Das S., Sardone A., Leroy A. K., Mathur S., Gallagher M., Pingel N. M., Pisano D. J., Heald G., 2020, ApJ, 898, 15
de Heij V., Braun R., Burton W. B., 2002, A&A, 391, 159

Di Cintio A., Knebe A., Libeskind N. I., Brook C., Yepes G., Gottlöber S., Hoffman Y., 2013, MNRAS, 431, 1220
Dolag K., Borgani S., Murante G., Springel V., 2009, MNRAS, 399, 497
Donnari M. et al., 2019, MNRAS, 485, 4817
Doumler T., Hoffman Y., Courtois H., Gottlöber S., 2013, MNRAS, 430, 888
Drake G. W., 1988, Can. J. Phys., 66, 586
Edlén B., 1979, Phys. Scr., 19, 255
Emerick A., Mac Low M.-M., Grcevich J., Gatto A., 2016, ApJ, 826, 148
Farber R., Ruszkowski M., Yang H.-Y. K., Zweibel E. G., 2018, ApJ, 856, 112
Faucher-Giguère C.-A., Lidz A., Zaldarriaga M., Hernquist L., 2009, ApJ, 703, 1416
Ferland G. J. et al., 2017, Rev. Mex. Astron. Astrofis., 53, 385
Fielding D. B., Bryan G. L., 2022, ApJ, 924, 82
Fillingham S. P., Cooper M. C., Pace A. B., Boylan-Kolchin M., Bullock J. S., Garrison-Kimmel S., Wheeler C., 2016, MNRAS, 463, 1916
Ford G. P. et al., 2013, ApJ, 769, 55
Ford A. B., Oppenheimer B. D., Davé R., Katz N., Kollmeier J. A., Weinberg D. H., 2013, MNRAS, 432, 89
Ford A. B., Davé R., Oppenheimer B. D., Katz N., Kollmeier J. A., Thompson R., Weinberg D. H., 2014, MNRAS, 444, 1260
Forero-Romero J. E., González R., 2015, ApJ, 799, 45
Fox A. J. et al., 2014, ApJ, 787, 147
Fraternali F., 2017, Gas Accretion via Condensation and Fountains. Springer International Publishing, Cham, p. 323
Fraternali F., Marasco A., Marinacci F., Binney J., 2013, ApJ, 764, L21
Froning C. S., Green J. C., 2009, Ap&SS, 320, 181
Furlong M. et al., 2015, MNRAS, 450, 4486
Garrison-Kimmel S., Boylan-Kolchin M., Bullock J. S., Kirby E. N., 2014, MNRAS, 444, 222
Giovanelli R. et al., 2013, AJ, 146, 15
Girichidis P., Naab T., Hanasz M., Walch S., 2018, MNRAS, 479, 3042
Górski K. M., Hivon E., Banday A. J., Wandelt B. D., Hansen F. K., Reinecke M., Bartelmann M., 2005, ApJ, 622, 759
Gottlöber S., Hoffman Y., Yepes G., 2010, in High Performance Computing in Science and Engineering, Garching/Munich 2009. Springer, Berlin, p. 309
Grand R. J. J. et al., 2017, MNRAS, 467, 179
Green J. C. et al., 2011, ApJ, 744, 60
Gronke M., Oh S. P., 2018, MNRAS, 480, L111
Gunn J. E., Gott J., Richard I., 1972, ApJ, 176, 1
Guo Q., White S., Li C., Boylan-Kolchin M., 2010, MNRAS, 404, 1111
Gupta A., Mathur S., Krongold Y., Nicastro F., Galeazzi M., 2012, ApJ, 756, L8
Hammer F., Yang Y., Fouquet S., Pawlowski M. S., Kroupa P., Puech M., Flores H., Wang J., 2013, MNRAS, 431, 3543
Hani M. H., Sparre M., Ellison S. L., Torrey P., Vogelsberger M., 2018, MNRAS, 475, 1160
Hani M. H., Ellison S. L., Sparre M., Grand R. J. J., Pakmor R., Gomez F. A., Springel V., 2019, MNRAS, 488, 135
Hausammann L., Revaz Y., Jablonka P., 2019, A&A, 624, A11
Hennawi J. F., Prochaska J. X., Cantalupo S., Arrigoni-Battaia F., 2015, Science, 348, 779
Herenz P., Richter P., Charlton J. C., Masiero J. R., 2013, A&A, 550, A87
Hoffman Y., Ribak E., 1991, ApJ, 380, L5
Hopkins P. F., Chan T. K., Ji S., Hummels C. B., Kereš D., Quataert E., Faucher-Giguère C.-A., 2020, MNRAS, 501, 3640
Hummels C. B., Bryan G. L., Smith B. D., Turk M. J., 2013, MNRAS, 430, 1548
Hummels C. B. et al., 2019, ApJ, 882, 156
Ibata R. A. et al., 2013, Nature, 493, 62
Irodotou D. et al., 2021, preprint (arXiv:2110.11368)
Jentschura U. D., Kotochigova S. A., Mohr P. J., Taylor B. N. et al., 2005, Energy Levels of Hydrogen and Deuterium.
Ji S. et al., 2020, MNRAS, 496, 4221
Johnson W., Soff G., 1985, At. Data Nucl. Data Tables, 33, 405
Johnson S. D., Chen H.-W., Mulchaey J. S., 2015, MNRAS, 449, 3263
Kanjilal V., Dutta A., Sharma P., 2021, MNRAS, 501, 1143
Kimble R. A. et al., 1998, ApJ, 492, L83
Klypin A., Kravtsov A. V., Valenzuela O., Prada F., 1999, ApJ, 522, 82
Knebe A., Libeskind N. I., Knollmann S. R., Martinez-Vaquero L. A., Yepes G., Gottlöber S., Hoffman Y., 2011, MNRAS, 412, 529
Lau M. W., Prochaska J. X., Hennawi J. F., 2016, ApJS, 226, 25
Lehner N., Howk J. C., Thom C., Fox A. J., Tumlinson J., Tripp T. M., Meiring J. D., 2012, MNRAS, 424, 2896
Lehner N. et al., 2013, ApJ, 770, 138
Lehner N., Wotta C. B., Howk J. C., O'Meara J. M., Oppenheimer B. D., Cooksey K. L., 2018, ApJ, 866, 33
Lehner N. et al., 2020, ApJ, 900, 9
Lewis A. R. et al., 2015, ApJ, 805, 183
Li Y., Bryan G. L., Quataert E., 2019, ApJ, 887, 41
Liang C. J., Chen H.-W., 2014, MNRAS, 445, 2061
Liang C. J., Kravtsov A. V., Agertz O., 2018, MNRAS, 479, 1822
Libeskind N. I., Yepes G., Knebe A., Gottlöber S., Hoffman Y., Knollmann S. R., 2010, MNRAS, 401, 1889
Libeskind N. I., Knebe A., Hoffman Y., Gottlöber S., Yepes G., 2011, MNRAS, 418, 336
Libeskind N. I. et al., 2020, MNRAS, 498, 2968
Lovell M. R. et al., 2017, MNRAS, 468, 4285
Lucchini S., D'Onghia E., Fox A. J., Bustard C., Bland-Hawthorn J., Zweibel E., 2020, Nature, 585, 203
Maloney P. R., Putman M. E., 2003, ApJ, 589, 270
Marinacci F., Pakmor R., Springel V., 2014, MNRAS, 437, 1750
Marinacci F., Sales L. V., Vogelsberger M., Torrey P., Springel V., 2019, MNRAS, 489, 4233
Martin W. C., Zalubas R., 1983, J. Phys. Chem. Ref. Data, 12, 323
McCourt M., Oh S. P., O'Leary R., Madigan A.-M., 2018, MNRAS, 473, 5407
McKee C. F., Williams J. P., 1997, ApJ, 476, 144
McLeod M., Libeskind N., Lahav O., Hoffman Y., 2017, J. Cosmol. Astropart. Phys., 2017, 034
McPartland C., Ebeling H., Roediger E., Blumenthal K., 2016, MNRAS, 455, 2994
Metuki O., Libeskind N. I., Hoffman Y., Crain R. A., Theuns T., 2015, MNRAS, 446, 1458
Miller M. J., Bregman J. N., 2015, ApJ, 800, 14
Moos H. W. et al., 2000, ApJ, 538, L1
Moster B. P., Naab T., White S. D. M., 2013, MNRAS, 428, 3121
Müller A. et al., 2020, Nature Astron., 5, 159
Münch G., Zirin H., 1961, ApJ, 133, 11
Nelson D. et al., 2019, MNRAS, 490, 3234
Nielsen N. M., Churchill C. W., Kacprzak G. G., Murphy M. T., 2013, ApJ, 776, 114
Nuza S. E., Dolag K., Saro A., 2010, MNRAS, 407, 1376
Nuza S. E. et al., 2013, MNRAS, 432, 743
Nuza S. E., Parisi F., Scannapieco C., Richter P., Gottlöber S., Steinmetz M., 2014, MNRAS, 441, 2593
Nuza S. E., Kitaura F.-S., Heß S., Libeskind N. I., Müller V., 2014, MNRAS, 445, 988
Nuza S. E., Scannapieco C., Chiappini C., Junqueira T. C., Minchev I., Martig M., 2019, MNRAS, 482, 3089
Ocvirk P. et al., 2020, MNRAS, 496, 4087
Oppenheimer B. D. et al., 2016, MNRAS, 460, 2157
Oppenheimer B., Schaye J., Crain R., Werk J., Richings A., 2017, MNRAS, 481, 835
Owers M. S., Couch W. J., Nulsen P. E. J., Randall S. W., 2012, ApJL, 750, L23
Pakmor R., Springel V., 2013, MNRAS, 432, 176
Pakmor R., Bauer A., Springel V., 2011, MNRAS, 418, 1392
Pakmor R., Springel V., Bauer A., Mocz P., Munoz D. J., Ohlmann S. T., Schaal K., Zhu C., 2016, MNRAS, 455, 1134
Pakmor R. et al., 2017, MNRAS, 469, 3185
Pakmor R., Guillet T., Pfrommer C., Gómez F. A., Grand R. J. J., Marinacci F., Simpson C. M., Springel V., 2018, MNRAS, 481, 4410
Pakmor R. et al., 2020, MNRAS, 498, 3125
Pawlowski M. S., Kroupa P., 2020, MNRAS, 491, 3042

Pawlowski M. S., Ibata R. A., Bullock J. S., 2017, ApJ, 850, 132
Peeples M. S., Werk J. K., Tumlinson J., Oppenheimer B. D., Prochaska J. X., Katz N., Weinberg D. H., 2014, ApJ, 786, 54
Planck Collaboration XVI, 2014, A&A, 571, A16
Poggianti B. M. et al., 2017, ApJ, 844, 48
Prochaska J. X., Hennawi J. F., 2008, ApJ, 690, 1558
Prochaska J. X. et al., 2004, ApJ, 611, 200
Putman M. E. et al., 2002, AJ, 123, 873
Rahmani S., Lianou S., Barmby P., 2016, MNRAS, 456, 4128
Rahmati A., Schaye J., Pawlik A. H., Raivcevic M., 2013, MNRAS, 431, 2261
Richter P., 2020, ApJ, 892, 33
Richter P., Sembach K. R., Wakker B. P., Savage B. D., Tripp T. M., Murphy E. M., Kalberla P. M. W., Jenkins E. B., 2001, ApJ, 559, 318
Richter P., Sembach K. R., Howk J. C., 2003, A&A, 405, 1013
Richter P., Paerels F. B. S., Kaastra J. S., 2008, Space Sci. Rev., 134, 25
Richter P., Charlton J. C., Fangano A. P. M., Bekhti N. B., Masiero J. R., 2009, ApJ, 695, 1631
Richter P., Wakker B. P., Fechner C., Herenz P., Tepper-Garcáa T., Fox A. J., 2016, A&A, 590, A68
Richter P. et al., 2017, A&A, 607, A48
Rupke D. S. N. et al., 2019, Nature, 574, 643
Salem M., Bryan G. L., Hummels C., 2014, ApJ, 797, L18
Salem M., Besla G., Bryan G., Putman M., van der Marel R. P., Tonnesen S., 2015, ApJ, 815, 77
Salem M., Bryan G. L., Corlies L., 2016, MNRAS, 456, 582
Samuel J. et al., 2020, MNRAS, 491, 1471
Sanders N. E., Caldwell N., McDowell J., Harding P., 2012, ApJ, 758, 133
Savage B. D. et al., 2000, ApJ, 538, L27
Savage B. D. et al., 2003, ApJS, 146, 125
Savorgnan G. A. D., Graham A. W., Marconi A., Sani E., 2016, ApJ, 817, 21
Scannapieco C., Creasey P., Nuza S. E., Yepes G., Gottlöber S., Steinmetz M., 2015, A&A, 577, A3
Schaye J. et al., 2015, MNRAS, 446, 521
Schiavi R., Capuzzo-Dolcetta R., Arca-Sedda M., Spera M., 2020, A&A, 642, A30
Sembach K. R. et al., 2000, ApJ, 538, L31
Sembach K. et al., 2003, ApJS, 146, 165
Sick J., Courteau S., Cuillandre J.-C., Dalcanton J., de Jong R., McDonald M., Simard D., Tully R. B., 2015, Galaxy Masses as Constraints of Formation Models, 311, 82
Simpson C. M., Pakmor R., Marinacci F., Pfrommer C., Springel V., Glover S. C. O., Clark P. C., Smith R. J., 2016, ApJ, 827, L29
Simpson C. M., Grand R. J., Gómez F. A., Marinacci F., Pakmor R., Springel V., Campbell D. J., Frenk C. S., 2018, MNRAS, 478, 548
Smith R. J. et al., 2010, MNRAS, 408, 1417
Somerville R. S., Davé R., 2015, ARA&A, 53, 51
Sorce J. G., 2015, MNRAS, 450, 2644
Sorce J. G., Courtois H. M., Gottlöber S., Hoffman Y., Tully R. B., 2013, MNRAS, 437, 3586
Sorce J. G. et al., 2015, MNRAS, 455, 2078
Sparre M. et al., 2015, MNRAS, 447, 3548
Sparre M., Hayward C. C., Feldmann R., Faucher-Giguère C.-A., Muratov A. L., Kereš D., Hopkins P. F., 2017, MNRAS, 466, 88
Sparre M., Pfrommer C., Vogelsberger M., 2019, MNRAS, 482, 5401
Sparre M., Pfrommer C., Ehlert K., 2020, MNRAS, 499, 4261
Speagle J. S., Steinhardt C. L., Capak P. L., Silverman J. D., 2014, ApJS, 214, 15
Spitzer L., Jr, 1956, ApJ, 124, 20
Springel V., 2010, MNRAS, 401, 791
Springel V., Hernquist L., 2003, MNRAS, 339, 289
Springel V., White S. D. M., Tormen G., Kauffmann G., 2001, MNRAS, 328, 726
Springel V., Di Matteo T., Hernquist L., 2005, MNRAS, 361, 776
Springel V., Pakmor R., Zier O., Reinecke M., 2021, MNRAS, 506, 2871
Sternberg A., McKee C. F., Wolfire M. G., 2002, ApJS, 143, 419
Stocke J. T., Keeney B. A., Danforth C. W., Shull J. M., Froning C. S., Green J. C., Penton S. V., Savage B. D., 2013, ApJ, 763, 148
Suresh J., Rubin K. H. R., Kannan R., Werk J. K., Hernquist L., Vogelsberger M., 2016, MNRAS, 465, 2966–2982
Suresh J., Nelson D., Genel S., Rubin K. H. R., Hernquist L., 2019, MNRAS, 483, 4040
Tabatabaei F. S., Berkhuijsen E. M., 2010, A&A, 517, A77
Tolstoy E., Hill V., Tosi M., 2009, ARA&A, 47, 371
Tonnesen S., Bryan G. L., 2021, ApJ, 911, 68
Torrey P., Vogelsberger M., Genel S., Sijacki D., Springel V., Hernquist L., 2014, MNRAS, 438, 1985
Tully R. B. et al., 2013, AJ, 146, 86
Tumlinson J. et al., 2011, Science, 334, 948
Tumlinson J. et al., 2013, ApJ, 777, 59
Tumlinson J., Peeples M. S., Werk J. K., 2017, ARA&A, 55, 389
Tuominen T. et al., 2021, A&A, 646, A156
Turk M. J., Smith B. D., Oishi J. S., Skory S., Skillman S. W., Abel T., Norman M. L., 2011, ApJS, 192, 9
Turner M. L., Schaye J., Steidel C. C., Rudie G. C., Strom A. L., 2015, MNRAS, 450, 2067
van de Voort F., Bieri R., Pakmor R., Gómez F. A., Grand R. J. J., Marinacci F., 2021, MNRAS, 501, 4888
van de Voort F., Springel V., Mandelker N., van den Bosch F. C., Pakmor R., 2019, MNRAS, 482, L85
van der Marel R. P., Fardal M., Besla G., Beaton R. L., Sohn S. T., Anderson J., Brown T., Guhathakurta P., 2012, ApJ, 753, 8
Vogelsberger M., Genel S., Sijacki D., Torrey P., Springel V., Hernquist L., 2013, MNRAS, 436, 3031
Vogelsberger M. et al., 2014a, MNRAS, 444, 1518
Vogelsberger M. et al., 2014b, Nature, 509, 177
Vogelsberger M., Marinacci F., Torrey P., Puchwein E., 2020, Nature Rev. Phys., 2, 42
Wakker B. P., York D. G., Wilhelm R., Barentine J. C., Richter P., Beers T. C., Ivezić Ž., Howk J. C., 2008, ApJ, 672, 298
Wakker B., Howk J. C., Chu Y.-H., Bomans D., Points S. D., 1998, ApJ, 499, L87
Wakker B. et al., 2003, ApJS, 146, 1
Wakker B. P. et al., 2007, ApJ, 670, L113
Weinberger R., Springel V., Pakmor R., 2020, ApJS, 248, 32
Werk J. K., Prochaska J. X., Thom C., Tumlinson J., Tripp T. M., O'Meara J. M., Peeples M. S., 2013, ApJS, 204, 17
Werk J. K. et al., 2014, ApJ, 792, 8
Westmeier T., Brüns C., Kerp J., 2005a, A&A, 432, 937
Westmeier T., Braun R., Thilker D., 2005b, A&A, 436, 101
Westmeier T., Staveley-Smith L., Calabretta M., Jurek R., Koribalski B., Meyer M., Popping A., Wong O., 2015, MNRAS, 453, 338
Wetzel A. R., Hopkins P. F., Kim J.-h., Faucher-Giguère C.-A., Kereš D., Quataert E., 2016, ApJ, 827, L23
Williams B. F., 2003, AJ, 126, 1312
Williams B. F., 2003, MNRAS, 340, 143
Woodgate B. E. et al., 1998, PASP, 110, 1183
Wright R. J., Lagos C. d. P., Power C., Correa C. A., 2021, MNRAS, 504, 5702
Yin J., Hou J. L., Prantzos N., Boissier S., Chang R. X., Shen S. Y., Zhang B., 2009, A&A, 505, 497
Zheng Y., Peek J., Putman M., Werk J., 2019, ApJ, 871, 35
Zonca A., Singer L., Lenz D., Reinecke M., Rosset C., Hivon E., Gorski K., 2019, J. Open Source Softw, 4, 1298

APPENDIX A: RADIAL GAS METALLICITY PROFILES

We obtain the radial gas metallicity profiles in spherical shells equally spaced in the logarithmic radius ($\log r$) for the HESTIA galaxies in Fig. A1. Overall, the gas metallicities for MW and M31 look similar. The HESTIA galaxies are metal-rich in the inner disc regions (3–10 times the solar metallicity inside 10 kpc), after which the metallicity drops sharply out to the CGM regions (as low as 0.2 times solar metallicity at 500 kpc). Beyond this point, the metallicities rise

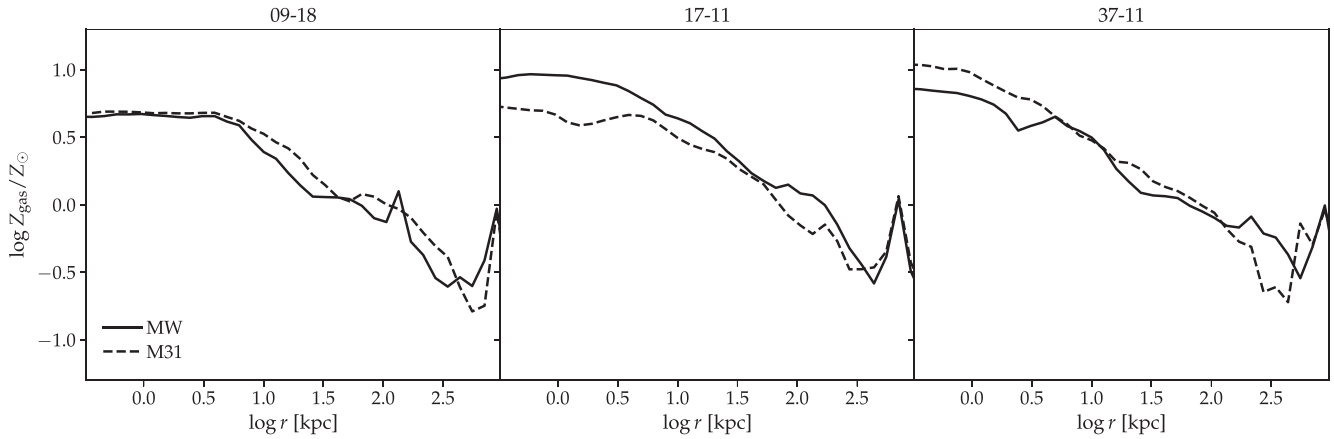

Figure A1. Radial gas metallicity profiles for the HESTIA galaxies. The profiles show two distinct regimes – metal-rich in the inner disc regions ($r < 10$ kpc) and metal-poor in the CGM regions ($r > 30$ kpc). The rise in metallicities at $r > 500$ kpc occurs due to the presence of the pairing galaxy at these distances.

again due to the presence of the pairing galaxy at those distances. As observed by Conroy et al. 2019, we also see our galaxies exhibiting a turn-over from being metal-rich (at $r < 10$ kpc) to metal-poor (at $r > 30$ kpc).

For the MW in 17–11 and M31 in 37–11 the central gas metallicities reach values as high as $10Z_\odot$. These values are clearly a factor of 2–3 higher than for M31 observations (Sanders et al. 2012), and these also exceed our expectations for MW-like galaxies (see fig. 10 in Torrey et al. 2014 for a compilation of observations of MW-mass galaxies). We therefore conclude that HESTIA produces a disc metallicity, which is up to a factor of 3 higher than expected from observations. There are no strong observational constraints on the MW and M31 CGM metallicity, but when comparing to observations we keep in mind the possibility that our simulations might have a CGM metallicity, which is up to a factor of 3 too high in comparison to *real galaxies*.

APPENDIX B: A LISTING OF THE MOST RELEVANT PARAMETERS FOR THE MOST MASSIVE GALAXIES IN EACH REALIZATION

In Table B1, B2, and B3 we show properties of the satellite galaxies in each of the simulations. The galaxy numbers appear in Fig. 1 of the main paper, and we see that all the dense H I regions are associated with one of the galaxies listed in the tables.

Table B1. A list of properties for the most massive galaxies in the 09–18 realization. Galaxy no. 0 corresponds to the M31, while galaxy no. 9 corresponds to the MW. Remaining galaxies can be correlated with their respective galaxy nos. in Fig. 1. Distance (kpc) refers to the distance of the corresponding galaxy from the LG centre, in kpc.

Galaxy no.	log M_* ($M_\odot$)	log M_{dm} ($M_\odot$)	log M_{gas} ($M_\odot$)	Dist. (kpc)
0	11.113	12.275	11.195	433.19
1	9.184	10.338	9.627	494.37
2	8.755	10.164	9.385	585.21
3	8.445	10.033	9.258	622.04
4	8.807	9.614	8.902	474.55
5	8.973	9.038	8.666	420.03

Table B1 – *continued*

Galaxy no.	log M_* ($M_\odot$)	log M_{dm} ($M_\odot$)	log M_{gas} ($M_\odot$)	Dist. (kpc)
6	8.665	9.540	8.636	478.16
7	7.854	9.729	8.453	328.25
8	8.189	9.098	7.599	335.97
9	10.911	12.156	11.078	433.19
10	10.390	11.111	10.207	554.78
11	9.220	10.345	9.707	658.60
12	8.896	10.254	9.596	767.30
13	9.026	9.952	9.503	415.00
14	8.640	10.133	9.419	547.98
15	8.718	9.748	9.207	525.90
16	8.012	9.907	8.967	549.84
17	7.983	9.771	9.025	152.61
18	8.638	9.469	8.839	420.42
19	6.909	9.152	8.151	572.19
20	7.010	9.237	7.800	684.53
21	7.769	9.052	7.444	508.79
22	5.203	9.241	5.246	421.25
23	8.181	9.944	9.138	387.82
24	7.261	9.910	8.785	683.50
25	7.389	9.822	8.931	641.68
26	7.497	9.556	8.419	658.64

Table B2. Same as B1, but for the 17–11. Galaxy no. 0 corresponds to the M31, while galaxy no. 1 corresponds to the MW.

Galaxy no.	log M_* ($M_\odot$)	log M_{dm} ($M_\odot$)	log M_{gas} ($M_\odot$)	Dist. (kpc)
0	11.079	12.310	11.212	338.01
1	11.062	12.184	10.919	338.00
2	9.648	10.330	9.422	455.76
3	8.985	10.429	9.697	259.56
4	8.686	10.282	9.745	244.43
5	9.461	10.074	9.414	306.94
6	8.745	10.304	9.593	640.84
7	8.977	10.023	9.619	114.45
8	9.334	9.702	8.899	389.40
9	8.469	9.654	9.248	233.49
10	8.195	9.843	9.044	409.12
11	8.029	9.246	8.753	240.47
12	7.028	9.620	8.369	263.22
13	6.871	9.401	8.495	422.59
14	7.285	9.435	8.344	336.52

Table B2 *– continued*

Galaxy no.	log M_* ($M_\odot$)	log M_{dm} ($M_\odot$)	log M_{gas} ($M_\odot$)	Dist. (kpc)
15	7.446	9.407	8.141	400.67
16	6.860	9.416	7.818	499.36
17	7.486	5.304	8.611	324.31
18	6.725	5.605	8.539	359.37
19	6.036	–	7.750	383.76
20	7.894	9.880	8.906	676.74
21	7.563	9.801	8.635	696.55
22	7.364	9.631	8.607	491.8
23	7.617	9.571	8.240	788.02
24	6.538	9.460	8.057	466.96
25	6.772	9.498	7.998	678.25
26	5.953	9.460	7.092	496.14

Table B3. Same as B1, but for the 37–11. Galaxy no. 0 corresponds to the M31, while galaxy no. 11 corresponds to the MW.

Galaxy no.	log M_* ($M_\odot$)	log M_{dm} ($M_\odot$)	log M_{gas} ($M_\odot$)	Dist. (kpc)
0	10.719	11.955	10.871	425.30
1	8.919	10.599	9.809	484.08
2	9.299	10.349	9.799	584.03
3	8.956	10.209	9.678	471.87
4	8.246	10.297	9.315	517.37
5	7.086	9.974	8.205	637.63
6	8.380	9.493	8.765	475.21
7	7.640	9.530	8.772	635.12
8	7.046	9.439	8.489	518.32
9	6.647	9.031	7.611	510.55
10	6.593	7.969	6.532	519.30
11	10.774	11.954	10.761	425.29
12	9.517	10.706	9.876	473.75
13	7.153	9.533	8.198	353.56
14	6.882	9.357	7.818	317.15
15	6.934	9.267	7.870	567.53
16	7.669	8.939	8.092	325.65
17	6.536	9.223	6.542	516.28
18	10.040	11.377	10.343	645.13
19	8.356	9.781	9.202	611.27
20	8.326	9.339	8.767	683.16
21	7.515	9.440	8.630	705.46
22	7.133	9.487	8.331	504.48
23	9.675	10.895	9.841	698.75
24	8.470	10.121	9.270	728.57
25	7.693	10.049	8.944	638.65
26	7.411	9.746	8.482	230.93
27	7.151	9.581	8.348	576.87
28	5.682	9.580	7.388	744.04
29	6.073	9.515	6.705	426.66
30	6.534	9.465	7.609	731.14
31	6.536	9.204	6.780	574.73

APPENDIX C: COLUMN DENSITY PROFILES FOR THE MW

In Fig. C1 we show the radial column density profile of the simulated MW for the different ions. This is complementary to the M31 column density profiles in Fig. 4.

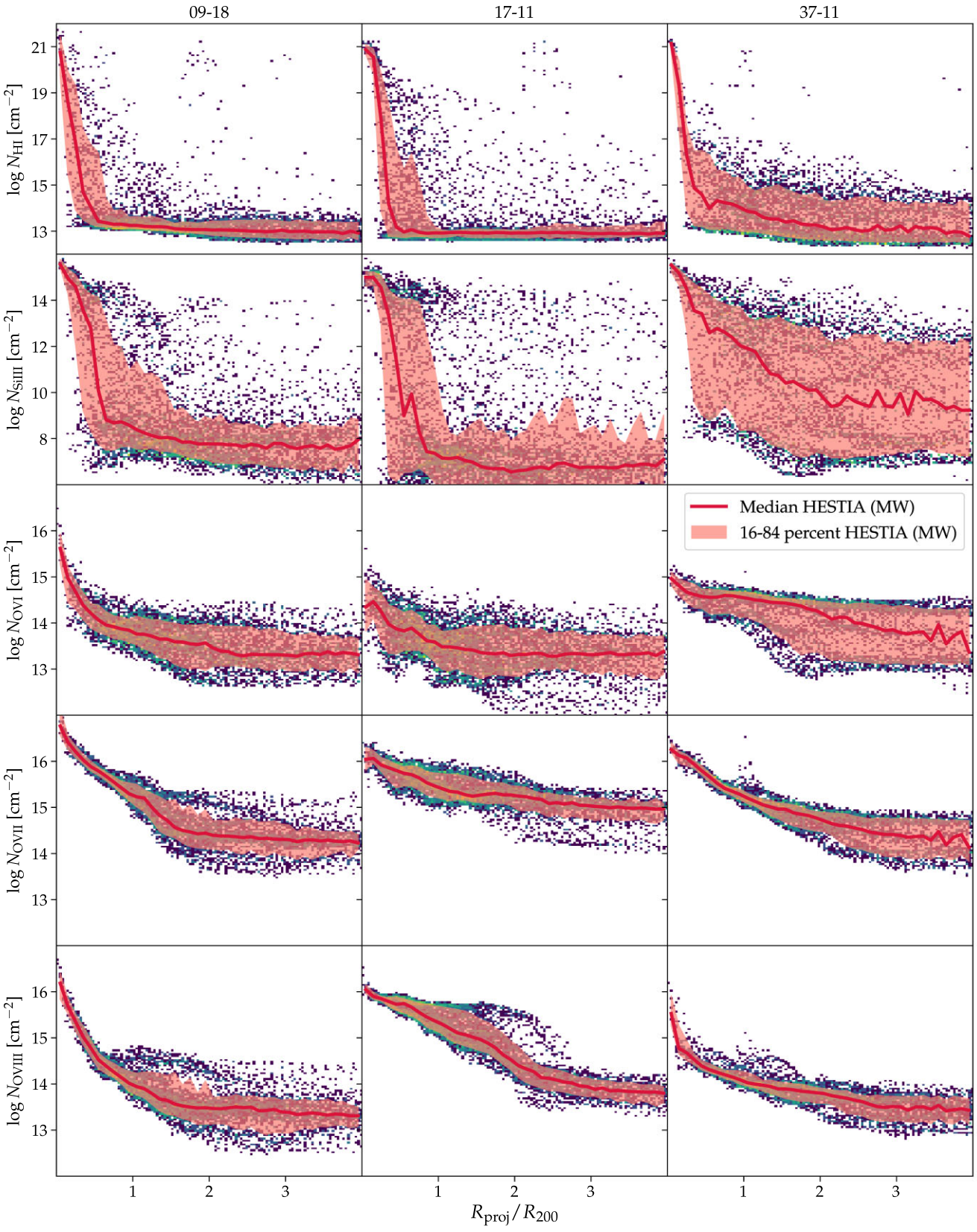

Figure C1. Same as Fig. 4, but for MW. A distinct blob of H I column density absorbers, which can be seen at a distance of ∼2.0 R_{200} in the H I profile for 09–18, can be correlated with the satellite galaxy numbered 17 in the corresponding skymap (H I skymap for 09–18 in Fig. 1).

APPENDIX D: CONVERGENCE TEST

We perform a convergence test, where we compare the high-resolution HESTIA simulations, which we presented in the main paper, to intermediate-resolution simulations with an eight times lower mass of the dark matter particles. In Fig. D1, we test whether the column density profiles of Si III and O VI are converged. In simulation 09–18, the column densities at $\gtrsim R_{200}$ are higher in the intermediate resolution simulation in comparison to the high-resolution simulations. For 17–11 and 37–11, we have the opposite trend – we see the highest column densities in the high-resolution simulations. The median profiles of O VI are only slightly affected by resolution with the difference between intermediate and high resolution simulations being less than a factor of two. We conclude that, on the whole, the column density profiles are well converged.

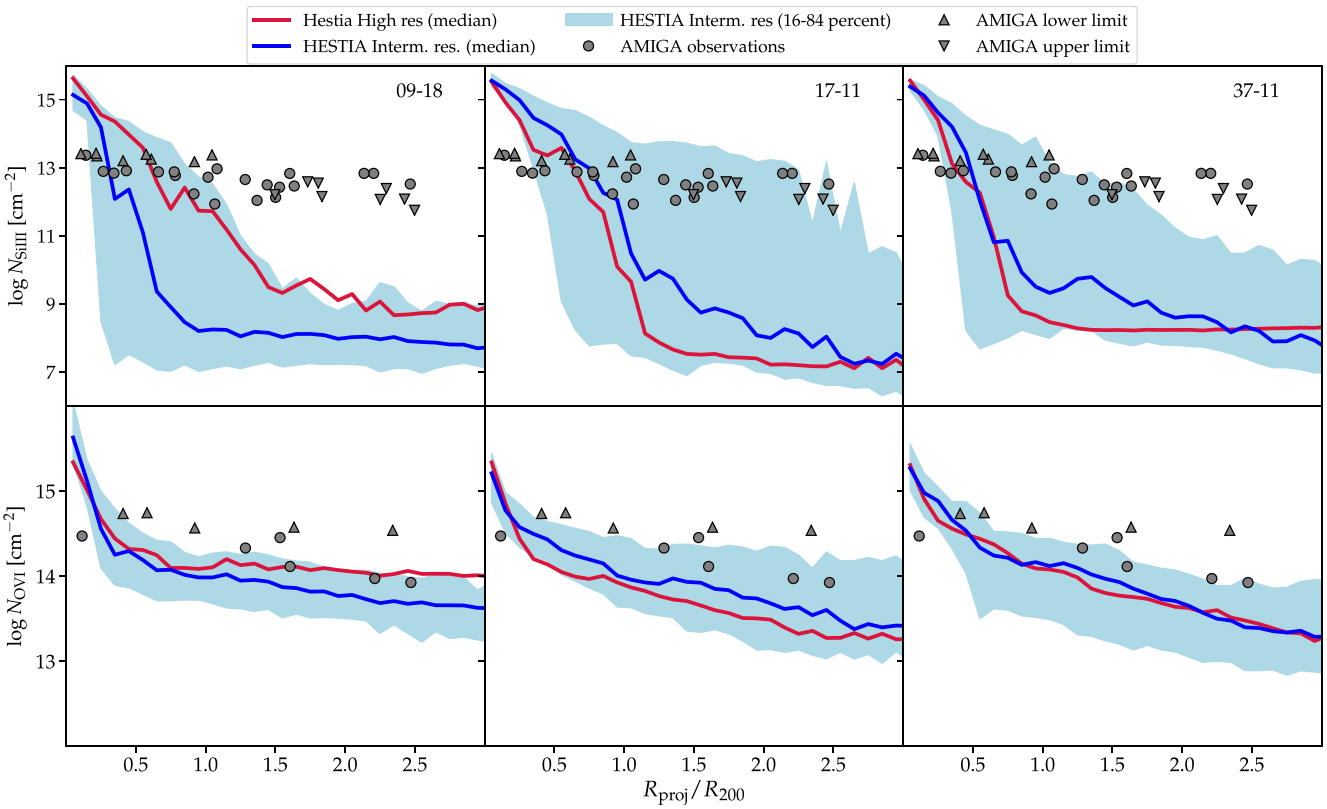

Figure D1. We perform a convergence test of Fig. 5. The thick red line shows the median of the high-resolution HESTIA simulations, which was also shown in Fig. 5. The blue line and contour show the median and 16–84 percentiles, respectively, of intermediate resolution simulations with an eight times lower mass resolution (dark matter particles have an eight times higher mass) in comparison to the high resolution simulations. Examination of the median profiles does not indicate a lack of convergence, so our column density profiles are well converged.

This paper has been typeset from a TEX/LATEX file prepared by the author.